A microchondrule-bearing micrometeorite and comparison with microchondrules in CM chondrites

Suttle, M.D.[1,2,3](*corresponding author*), Genge, M.J.[2,3], Salge, T.[4], Lee, M.R[5], Folco, L.[1], Góral, T. [4], Russell, S.S.[3] , Lindgren, P.[6]
martindavid.suttle@dst.unipi.it, m.genge@ic.ac.uk, t.salge@nhm.ac.uk, martin.lee@glasgow.ac.uk, luigi.folco@unipi.it, t.goral@nhm.ac.uk, sara.russell@nhm.ac.uk, paula.lindgren@geol.lu.se

[1.]Dipartimento di Scienze della Terra, Università di Pisa, 56126 Pisa, Italy
[2.]Department of Earth Science and Engineering, Imperial College London, South Kensington, London, SW7 2AZ, UK
[3.]Mineral and Planetary Sciences, The Natural History Museum, Cromwell Rd, London SW7 5BD, UK
[4.]Imaging and Analysis Centre, Core Research Laboratories, The Natural History Museum, Cromwell Rd, London SW7 5BD, UK
[5.]School of Geographical and Earth Sciences, University of Glasgow, Glasgow G12 8QQ, UK
[6.]Earth Science and Physical Geography, Lund University, 221 00 Lund, Sweden.

Abstract

We report the discovery of a partially altered microchondrule within a fine-grained micrometeorite. This object is circular, <10µm in diameter and has a cryptocrystalline texture, internal zonation and a thin S-bearing rim. These features imply a period of post-accretion parent body aqueous alteration, in which the former glassy igneous texture was subject to hydration and phyllosilicate formation as well as leaching of fluid-mobile elements. We compare this microchondrule to three microchondrules found in two CM chondrites: Elephant Moraine (EET) 96029 and Murchison. In all instances, their formation appears closely linked to the late-stages of chondrule formation, chondrule recycling and fine-grained rim accretion. Likewise, they share cryptocrystalline textures and evidence of mild aqueous alteration and thus similar histories. We also investigate the host micrometeorite's petrology, which includes an unusually Cr-rich mineralogy, containing both Mn-chromite spinel and low-Fe-Cr-rich (LICE) anhydrous silicates. Because these two refractory phases cannot form together in a single geochemical reservoir under equilibrium condensation, this micrometeorite's accretionary history requires a complex timeline with formation via non-equilibrium batch crystallization or accumulation of materials from large radial distances. In contrast, the bulk composition of this micrometeorite and its internal textures are consistent with a hydrated carbonaceous chondrite source. This micrometeorite is interpreted as a fragment of fine-grained rim material that once surrounded a larger parent chondrule and was derived from a primitive carbonaceous parent body; either a CM chondrite or Jupiter family comet.

***Keywords**: micrometeorites, microchondrules, CM chondrites, nebula condensates, EDX techniques*

Introduction

Micrometeorites are cosmic dust grains, <2mm in diameter, that originate from asteroids and comets (Kurat et al., 1994; Engrand and Maurette, 1998; Genge et al., 2008; Rubin and Grossman, 2010). Most particles are fragments of chondritic parent bodies and are, therefore, composed of either fine-grained volatile-rich matrix or are coarse-grained aggregates containing anhydrous silicates.

Respectively, these represent samples of altered matrix from CM, CR, CI and ungrouped C2 parent bodies (Taylor et al., 2012; Suttle et al., 2018) as well as disintegrated chondrules with affinities to both ordinary and carbonaceous chondrites (Genge et al., 2005; Genge, 2008; van Ginneken et al., 2012). The fine-grained micrometeorite class – to which the micrometeorite described here belongs – represent up to 75% of the flux (Taylor et al., 2012), are typically small (<250µm in size, at the lower end of the micrometeorite's size range) and may originate primarily from the recently disrupted (~8.5Ma, Nesvorný et al., 2006) Veritas asteroid family.

Fine-grained micrometeorites are dominated by clusters of Fe and Mg-bearing phyllosilicates (Noguchi et al., 2002; Sakamoto et al., 2010). However, these typically have experienced dehydroxylation, solid-state recrystallization and potentially partial melting during their passage through Earth's atmosphere. Thus, their matrices commonly appear as a fused, porous groundmass of micro-crystalline olivine. However, in most instances, this matrix preserves the pre-atmospheric texture of their parent body (Genge et al., 1997; Suttle et al., 2017a) whilst also retaining some unaltered relict crystals. Consequently, small (4-10µm) high-Mg olivine and pyroxene crystals are common (Imae et al., 2013) and may show fragmented angular morphologies or rounded residual morphologies, the latter of which attests to advanced aqueous alteration whilst on their parent asteroid (Suttle et al., 2018). Accessory Fe-oxides, Fe-sulfides and thermally altered organics are also common (Suttle et al., 2017a).

Upon liberation from their parent body, cosmic dust rapidly (<10Ma) spirals into the inner solar system, losing angular momentum as radiation pressure exerts a force tangential to their orbit (Wyatt and Whipple 1950; Gonczi et al., 1982). This delivery mechanism, referred to as Poynting–Robertson (P-R) drag ensures that all mm-scale cosmic dust is ultimately either captured by the terrestrial planets or consumed by the Sun (Vokrouhlický et al., 2008). Thus, micrometeorites sample a large and significantly more diverse population of solar system small bodies – all those which are actively producing dust – meanwhile, their larger meteorite counterparts are transported to Earth by a restrictive set of mechanisms, including mean motion resonances with planets (Farinella et al., 1993) and by Yarkovsky drift (Vokrouhlický et al., 2000). This process means that they are derived from a limited number of parent bodies (~110-150, Greenwood et al., 2017). Consequently, the study of micrometeorites provides a diverse sample of extraterrestrial material both related to existing meteorite groups and including exotic materials that would otherwise remain unsampled and unstudied.

Carbon-rich micrometeorites, characterised by extreme deuterium excesses (Duprat et al., 2010), and containing glass with embedded metal sulfides (GEMS) and primitive nebular condensates (Noguchi et al., 2017) are currently associated with distant cometary parent bodies, formed beyond the nitrogen snow line (Dartois et al., 2013; 2018). These particles are termed ultracarbonaceous Antarctic micrometeorites [UCAMMs] (Dobrică et al., 2009; Duprat et al., 2010; Imae et al., 2013; Noguchi et al., 2017; Yabuta et al., 2017) and provide a compelling example of how extraterrestrial dust has expanded our collective inventory of solar system materials. Likewise, unique micrometeorites with asteroidal affinities are also known; these include a fragment of basaltic crust derived from a differentiated protoplanet (Gounelle et al., 2009), a polycrystalline, fine-grained micrometeorite exhibiting evidence of flash heating and quench cooling whilst in space (Noguchi et al., 2013) and an unusually Ni-rich, oxidised and irradiated giant micrometeorite with possible affinities to the CK chondrite class (Cordier et al., 2018).

Furthermore, a population of cosmic spherules with an unusual ^{16}O-poor isotopic signature have also been described (Suavet et al., 2010; van Ginneken et al., 2017). These exotic micrometeorites may represent up to 12% of the micrometeorite flux at coarse size fractions (>300µm, van Ginneken et al., 2017) and appear to sample a new chondrite class, potentially related to the ordinary chondrites, but currently lacking unmelted and well-characterised representatives.

In this study we investigate a single fine-grained Antarctic micrometeorite from the Cap Prud'homme blue ice collection (CP94-050-182, Fig.1, ~100µm). This particle was recovered during the 1994

expedition (Maurette et al., 1991) and picked from filter residues by M. Genge and later analysed as part of M. Suttle's PhD thesis (2014-2018). We selected this particle for a detailed study owing to the presence of a microchondrule (7µm diameter, Fig.1) – the first reported occurrence within a micrometeorite. To date, microchondrules within hydrated chondritic parent bodies are essentially unstudied and are, therefore, in need of characterisation and investigation. Consequently, we provide data from three microchondrules within CM chondrites (Murchison and EET 96029) for comparison. In addition, the host micrometeorite is also unusual with respect to its apparent Cr-enriched mineralogy, this is combined with textural features implying a significant period of parent body aqueous alteration and a diverse array of both high and low-temperature phases, requiring a complex geological history.

Microchondrules, current perspectives: Chondrules are spherical igneous droplets, composed of anhydrous silicates, FeNi-sulfides, native metal and mesostasis glass (Hewins, 1997; Wasson, 1993). Their internal textures are porphyritic, single-crystal or cryptocrystalline and their exteriors may be mantled by successive fine or coarse-grained, concentric rims (Rubin, 1984). Microchondrules are a subset of chondrules which, by definition, are <40µm in diameter (Krot and Rubin, 1996; Krot et al., 1997). They represent the predominant chondrule type among the unusual metal-rich CH chondrites (Krot et al., 2005a; 2007) whilst also being common components within the rims of larger chondrules and are especially abundant in the ordinary chondritic meteorites (Krot et al., 1997; Bigolski et al., 2016). Furthermore, microchondrules are found within the anhydrous CO (ALH 77003, Kainsaz and Lancé) and CV (Vigarano and Allende) chondrites but as relatively minor components (Fruland et al., 1978; Rubin et al., 1982). Finally, microchondrules have been reported from cometary materials, including the STARDUST mission samples (Zolensky et al., 2008) and in one UCAMM (Fig.5 in Noguchi et al., 2017). In contrast, the prevalence, and petrology of microchondrules in hydrated chondrites remains largely unstudied. To our knowledge no publication has yet examined microchondrules in CM chondrites and only a single study describes microchondrules from CR chondrites (Weisberg et al., 1993) although using a different definition (<200µm) and providing limited petrographic details. Thus, the occurrence of microchondrules in hydrated chondrites remains largely unreported and this lack of study further extends to microchondrules in hydrated fine-grained micrometeorites.

The formation mechanisms for microchondrules remain a matter of debate and likely involve several distinct processes. In the CB-CH chondrite clan microchondrule formation is, however, well-constrained and appears to have occurred by crystallization from a vapour-melt plume after single high-energy planetesimal-scale collision (Krot et al., 2005a). In contrast, most microchondrules appear to have formed in the solar nebula through localized flash melting events, either by limited melting at chondrule margins or by wholesale melting of chondrules and shearing of droplets from the main body. In each case, resulting in the generation and capture of smaller molten droplets. This formation hypothesis is based on the co-occurrence of microchondrules within the fine-grained rims of normal-sized chondrules and on the close geochemical and textural similarities between microchondrules and their host chondrule parents (Wasson et al., 1995; Krot et al., 1997; Krot and Rubin, 1997; Wasson and Rubin, 2009; Bigolski et al., 2016). Several transient heating mechanisms are currently suggested, including spallation within nebula shock waves (Bigolski et al., 2016), splattering events, occurring when molten chondrules collide (Dobrică et al., 2016) and electrical discharge sheets, generated by the thermal ionisation of alkali metals (Bigolski et al., 2016). Thus, most models propose that heating occurred within the solar nebula and assume that microchondrule formation and chondrule formation were synchronous. The later aqueous alteration of microchondrules whilst on their parent body has also gained interest recently with new studies describing the reprocessing of non-porous igneous glass microchondrules in LL3.0 Semarkona, resulting in oxidation without significant geochemical exchange (Dobrică et al., 2018).

Methods

Geochemical analysis was conducted at the Natural History Museum (NHM), London in the Imaging and Analysis Centre. The micrometeorite was analysed using backscatter electron (BSE) imaging, standards-based energy dispersive X-ray (EDX) spectrometry and high-spatial resolution X-ray elemental mapping. Later, we performed high-resolution BSE imaging and standardless EDS spot analyses on features of interest within the particle's matrix at the University of Pisa's Interdepartmental centre for science and engineering (CISIM). Meanwhile, geochemical and textural data were collected on microchondrules within the CM chondrite's Murchison and Elephant moraine (EET 96029) at the School of Geographical and Earth Sciences, University of Glasgow.

Micrometeorite analysis: A Zeiss EVO 15LS scanning electron microscope (SEM) fitted with an Oxford Instruments' 80mm^2 X-Max silicon drift detector (SSD) energy dispersive spectrometer provided quantitative geochemical assays. All analyses were performed under high-vacuum and at a fixed working distance of 8.5mm (this being the optimal sample-to-pole-piece distance to maximise X-ray counts at the EDS detector on this instrument). An electron beam accelerating voltage of 20kV and beam current of 3nA were used, resulting in an output count rate of approximately 9kcps for silicate minerals. Spectra were acquired under process time '5', with ~28% deadtime and at 60s acquisition time. The beam current was routinely monitored using the built-in Faraday cup to ensure analysis conditions remained stable. Prior to analysis, the EDX system was calibrated (for gain and energy channel) using a polished cobalt metal reference and the resulting EDX data processed using the Oxford Instruments INCA software. Standards-based quantification was performed using calibrated reference samples and applying standard XPP matrix correction routines (Wendt and Schmidt, 1978). Weight total were determined as oxide% by calculating "*oxygen by stoichiometry*" for each cation. The accuracy and precision for major rock-forming silicate cations were cross-checked against analyses on the Smithonian Kakanui augite reference standard, whose composition is known from dissolution. Element detection limits are on the order of 0.1-0.3wt%, while analytical uncertainties have a relative error dependent on the element's concentration. For major elements (>10wt%) uncertainties vary by 1-3wt%, for minor elements (>1-10wt%) uncertainties are ~10% and for trace elements (<2wt%) uncertainties are ~30-50%.

X-ray microanalysis techniques can only quantify volumes of homogenous composition, using a matrix correction which corrects theoretical peak intensities for inter-element affects (atomic number, absorption, fluorescence). Quantification accuracies are therefore compromised where EDS analyses are conducted on an area of mixed phase composition (Dalton and Lane, 1996; Llovet et al., 2012). This is a long-standing problem for the use of EDS and EMPA on small and complex mineral assemblages and is especially problematic in planetary sciences where mineral phases in chondritic samples are commonly <10µm in size, heterogeneously mixed and, thus, form assemblages with large local variations in (atomic) density. Their analysis can result in secondary (X-ray) fluorescence effects leading to the generation of additional X-rays, within the interaction volume where the K, L and M-lines of light elements are excited by X-rays emitted from elements which have previously been excited by primary interaction with the electron beam. In this study we attempted to analyse only homogeneous areas, however, this is not always possible where the size of the electron beam spot and the interaction volume within the sample is significantly larger than the phase under analysis. This is also unavoidable in the bulk analysis of the particle's sub-micron-sized matrix (Table.1: A19-A22) but also for some spot analyses, such as on the Mn-chromite spinels (Table.1: A17, A18) which inevitably suffer from electron beam overlap and, therefore, carry higher analytical errors.

To better identify micron-scale phases, embedded within the sample's complex matrix, we used a FEI Quanta 650 field emission SEM, equipped with an annular Bruker Flat Quad EDS SDD. Initially, a hyperspectral imaging dataset that provided complete spectra for each pixel of the SEM image was acquired over the entire micrometeorite's exposed cross section. This was ran for 60 minutes at 0.18µm pixel resolution, ~28.9kcps and dead times of 5-10 % using an accelerating voltage of 12kV. The element identification was improved by use of the Maximum Pixel Spectrum function (Fig.4, Bright and Newbury, 2004). This function generates a synthetic spectrum, composed of the highest count

level for each spectrum energy channel in the hyperspectral imaging dataset and ensures detection of elements that occur even in only a single pixel of an element map (Bright and Newbury, 2004; Merlet and Llovet, 2012; Salge et al., 2017). Spatially-resolved elemental X-ray maps (Fig.2) and area spectra were extracted from this dataset.

To further resolve the unusual micron-sized spherical inclusion (subsequently interpreted as a microchondrule) and its surrounding matrix geochemistry an ultra-high spatial resolution X-ray map was produced under experimental, intermediate-voltage conditions (Fig.3). An acceleration voltage of 9kV was employed. At lower voltages, the interaction volume induced by the electron beam is significantly reduced. This has the effect of increasing the spatial resolution; allowing smaller features to be resolved (Merlet and Llovet, 2012; Burgess et al., 2013). Because the microchondrule in CP94-050-182 has a diameter of just 7µm, and since the BSE data indicated geochemical variations within this object at a sub-micron scale, an experimental procedure was employed to resolve these features. At 9kV and an acquisition time of 16 hours and 19 minutes, an output count rate of ~6.2kpcs and deadtimes around 0% were achieved, generating a hyperspectral imaging dataset with a pixel size of just 22nm. Element maps in Fig.3 are displayed as net intensity maps, generated using an automatic routine which deconvolutes energy peaks with overlapping element lines (e.g. Fe-L, Cr-L) using a physical background subtraction (Wendt and Schmidt, 1978) and a least square fit with stored line profiles. However, we also independently estimated the effective depth of emitted X-rays and the associated radial resolution for the EDX map to determine how the electron beam interaction volume compares to the sampling resolution in the presented image. For this we used the CASINO software [v2.4.8.1] (Drouin et al., 2007) to model the beam-sample interaction. Here we defined a substrate using the bulk microchondrule composition obtained by the high voltage standards-based EDS analysis. (For further details see the supplementary material S1.) This model revealed a 400nm X-ray emission depth and a 100nm radial resolution. Since, the pixel size of an image should be at least twice as high as the spatial resolution (due to the Nyquist Limit) the pixel size used in the EDX map sufficiently oversamples the map's true spatial resolution ensuring no data is lost (this is further explained in the supplementary materials).

However, the use of intermediate acceleration voltages to obtain significantly higher spatial resolution ultimately also results in compromised quantification accuracies. This is because the optimum overvoltage ratio ($U=E_0/E_c$) required to fully excite a given element line is approximately 2-3 times the critical energy (E_c) (Merlet and Llovet, 2012). Thus, the 9kV beam employed here carries insufficient energy to fully excite the K α-lines of elements with an atomic number Z>20 (Ca E_cK=4.03keV (Merlet and Llovet, 2012). To counteract this problem the Bruker software uses a lower overvoltage ratio (1.4x the E_c), which can be applied to elements that have relatively high concentrations in the sample under analysis. In the present study, the (lower intensity) K-lines of Ti (E_cK = 4.996 keV) and Cr (E_cK = 5.989 keV) were suitable for analysis, while the remaining transition elements (Mn, Fe and Ni) were analysed using their lower intensity L-line families. Using L-lines for quantification is, similarly, problematic owing to their lower peak-to-background ratios and the effects of peak overlap – where the L-lines of transition elements are partially obscured by the higher-signal K-lines of lighter elements (Merlet and Llovet, 2012). Thus, the quantification of the transition elements (at low and intermediate voltages) is, therefore, particularly challenging. For the lowest energy range (<1keV), L-line absorption edges lie within the bremsstrahlung background and, thus, the energy dependence of the efficiency and the uncertainties of absorption effects result in significantly higher errors (Pinard et al., 2015).

The two geochemical analysis methods described above are critically evaluated in this study. We compare the calculated bulk compositions of the micrometeorite-hosted microchondrule determined using conventional high voltage standards-based EDS (collected on the Zeiss EVO) against the composition determined by intermediate voltage standardless EDS analysis from the hyperspectral imaging dataset (Fig.5 and Table.1: A1 & A2). Data obtained from the annular-Bruker SDD is highly sensitive to surface features, and under conditions in this study has a maximum penetration depth up to 670nm. By contrast, the estimated penetration depth of the high voltage standards-based EDS

(EVO) spot analysis is significantly deeper at ~3µm and therefore might be considered a more accurate approximation of the spherical inclusion's (microchondrule's) bulk composition. Furthermore, the spot analysis obtained by EDS, was performed under conventional operating conditions (as explained above) and therefore provided sufficient acceleration voltages to fully excite the K α lines of all elements. However, under long analysis times and/or high-voltage conditions, volatile alkali elements, such as Na and K, are susceptible to loss by migration, especially when hydrous silicate glasses are analysed. Therefore, both analyses may under-estimate the true concentrations of Na and K (Morgan and London, 1996; 2005). Thus, the discrepancy between the two datasets can be understood as a product of differing analytical times, electron beam conditions, interaction volumes and quantification procedures. Despite these many different variables, the two compositions we derive for the microchondrule (bulk) are very similar, suggesting that we are approaching close to the true composition.

Mid-IR micro-spectroscopic data were collected at The Diamond Lightsource, synchrotron science facility, located in the Harwell Science and Innovation Campus, Oxfordshire, UK. A global mid-IR spectrum (Fig.6) was collected from CP94-050-182 using a rectangular aperture, whose slit size was altered to fit the geometry of the micrometeorite. Further details of the analytical conditions and post-processing data handling are outlined in Suttle et al., (2017a).

Analysis on CM chondrites: Two CM chondrites, Murchison and EET 96029, were also analysed for comparison. We searched their matrices for microchondrules and identified three objects. Two microchondrules in Murchison were analysed under SEM-EDS at the University of Pisa. The EET 92029 microchondrule was studied by SEM and transmission electron microscopy (TEM) at the University of Glasgow. The SEM imaging used a FEI Quanta operated at 20kV. An electron-transparent sample of the microchondrule and associated fine-grained rim was prepared for TEM work using a FEI Duomill focused ion beam (FIB) instrument operated using 30kV Ga^+ ions. Bright-field TEM images and selected area electron diffraction (SAED) patterns were then obtained from the ~100 nm thick sample using a FEI T20 TEM operated at 200kV. Further details of the FIB and TEM procedures, and the EET 96029 meteorite, are provided in Lee et al. (2016). The two microchondrules from Murchison were analysed under SEM-EDS at the University of Pisa to obtain high-resolution BSE images and geochemical compositions.

Results

CP94-050-182: This particle (Fig.1) is a small (78x108µm), fine-grained Antarctic micrometeorite, containing a partial magnetite rim and no igneous rim. Dehydration cracks are common, appearing as long (>50µm), relatively wide (~3µm) voids, which are broadly orientated NE-SW (with respect to an arbitrary vertical "North"), or as many small (4µm) clustered cracks. The particle's global mid-IR spectrum (Fig.6.) reveals only an olivine signature, implying that this micrometeorite contains a groundmass dominated by fine-grained olivine, although glass may also be present.

The internal mineralogy is characterised by a heterogeneous mix of anhedral minerals (>2.5µm) and clustered mineral aggregates (<20µm, Fig.1C-F), suspended within a porous matrix (Fig.1I, 1J). This includes low-Fe (<2.5wt%), High-Ca (12-18wt%) pyroxenes (Fig.1C, Fig.7, Table.1: A3-A5) with diopside compositions and containing high trace element concentrations, Al (2.1-2.9wt%) and Ti (0.4-0.5wt%) but especially notable for their elevated Mn and Cr: Mn (0.8-1.7wt%) and Cr (consistently 1.4wt%). In addition, low-Ca pyroxene (enstatite, En67-71, Fs29-33, Wo0-1) were also identified (Fig.1D, 1I and Table.1: A6, A7), meanwhile, olivine is common (Fig.1E, 1G, 1H, 1L and 1M & Table.1: A8-A12) as both fayalite (Fo39-41) and forsterite (Fo67-88). Fayalites have detectable Na (<0.3wt%), S (0.2-0.3wt%) and Ti (<0.3wt%) as well as relatively high Al concentrations (2.0-2.8wt%). In contrast, forsterites contain detectable P (0.1-0.2wt%), Cl (<0.2wt%) Ca (0.1-0.2wt%) and Zn (0.8wt%) and have Cr concentrations up to 1.2wt% and Mn up to 0.4wt%. These anhydrous silicates are commonly surrounded by a thick irregular-shaped and coarse-grained phase with a non-stoichiometric Fe-rich

composition (Table.1: A13, A14 & A19). In this micrometeorite, micron-scale Mn-bearing (Mn: 6.6-7.8wt%) chromite spinels (Table.1: A17, A18 – Cr: 19-40wt%, Al: 0.4-1.0wt%) are an accessory phase. Their presence is unusual in fine-grained micrometeorites, where chromite and Cr-spinels are either absent or extremely rare (Genge et al., 2008).
Elemental X-ray mapping (Fig.2) reveals the presence of a single Fe, Al, Ca and Ti hotspot with a broadly triangular shape (20x30µm in size) and with a two-phase non-stochiometric composition (Fig.1F, Fig.2D, 2E, 2H and Table.1: A13-A16). This region can be separated into an Fe-rich phase, with close similarities to the other Fe-rich regions described above that mantle the anhydrous silicates and a Ca-Al-Ti-rich glass (Ca: 17.8-24.4wt%, Al:2.3-6.2wt% & Ti:0.8-1.4wt%). Such high concentrations of refractory elements represent early-formed, high-temperature CAIs (Ca-Al rich inclusions). Finally, the lower portion of this micrometeorite (Fig.1A, highlighted) is geochemically and textural distinct from the main mass (compare Fig.1I and 1J). This region has a Mg-enriched (13.7wt%), Al-depleted (~1.0wt%) composition (Table.1: A21 vs. A19, A20) abundant Cr-spinels and a greater proportion of the clustered, small dehydration cracks (Fig.1A, 1J). The contact between this domain and the rest of the micrometeorite is gradational over a width of 5µm.

Although the bulk matrix composition is chondritic (Fig.5A, Table.1: A22), notable depletions and enrichments are observed. Both Ni and S are depleted, by approximately 1 order of magnitude relative to solar values. This trend is common among the Cap Prud'homme micrometeorites and reflects the leaching of highly mobile, soluble phases during interaction with terrestrial water (Kurat et al., 1994). Exposure could have occurred either during prolonged contact with Antarctic blue ice or during their extraction from the ice (Duprat et al., 2007). Additionally, a weak trend of increasing elemental abundance with increasing volatility is present, with progressive enrichments observed from Al to Zn (Fig.5A).

CP94-050-182 contains a microchondrule (Fig.1B, 7µm in diameter), located near to its perimeter. This microchondrule has a chondritic and mildly volatile-enriched composition (Fig.2, Fig.5B, Fig.9 and Table.1: A1, A2) and a cryptocrystalline texture. There is a good agreement between the two bulk compositions analyses (high and intermediate voltage assays) for major elements (with abundances >2wt%). Refractory Al and Ca and the moderately refractory Mg, Fe, Cr and Si are present at chondritic abundances, while Na and K concentrations are elevated relative to chondritic compositions in both assays (Na: 6.50x and 1.43x, K: 16.90x and 2.68x respectively). However, the high voltage EVO analysis consistently overestimates the concentration of volatile and moderately volatile elements (Na, K, Cl, Mn and Zn) when compared to the standardless intermediate voltage analyses (Fig.5B and Table.1). Thus, relative to the CI Ivuna standard, Na, K and Cl concentrations are elevated by up to an order of magnitude above chondritic values although true values are likely to be closer to chondritic. The microchondrule's internal texture is extremely fine-grained, composed of submicron crystals and contains geochemical heterogeneities (Fig.3). The microchondrule core is irregular in shape and EDX maps reveal moderate enrichment in Si, relative to the margin. In addition, several ~500nm size Ca-rich phases are located in the core (Fig.3A). Conversely, the microchondrule's margins are elevated in Fe and surrounded by a 300nm thick S-bearing rim (Fig.3B), resulting in a sharply defined contact with the matrix of the host micrometeorite.

Microchondrules in CM chondrites: Three microchondrules were found within the fine-grained matrix of two CM chondrites (Fig.10). Each microchondrule is located within the rim of a coarse-grained component; either a CAI, as in EET 96029, or within chondrule rims or compound chondrule rims (Fig.10H), as in Murchison. They have diameters of 3.5-5µm and well-defined boundaries. The microchondrule in EET 96029 has a subtle internal zonation allowing a separate core and margin to be distinguished (Fig.10B). In contrast, the two microchondrules in Murchison have clear internal compositional variations with notable changes in mean atomic number outward from the core, to a marginal zone and finally to an outer rim (Fig.10I and J). A bulk chemical composition was collected for one of the Murchison microchondrules (Fig.5B, Table.1: B1, Fig.10I) showing a chondritic

composition with similar abundances of refractory and moderately refractory elements (Al, Ca, Si, Mg, Fe, Cr and Mn) to the microchondrule in CP94-050-182. Although the volatile budget for the CM microchondrule includes relatively high Na concentrations (1.2wt%), other volatile elements, such as K and Cl were not detected. However, this most likely reflects differences in the quality and analytical capabilities of the two different instruments used to measure the different microchondrules; with significantly less sensitive (higher) detection limits for the standardless intermediate voltage system (FEI 450) than for the standards-based high voltage Zeiss EVO.
For the microchondrule in EET 96029, TEM imaging (Fig.10A-G) revealed a transitional boundary between the microchondrule and host matrix on the nano-scale (Fig.10E) and a poorly crystalline structure (Fig.10G). The SAED obtained from the microchondrule shows that it is composed of phyllosilicates that are poorly crystalline (i.e., with only short-range order) and randomly oriented.

Discussion

Micrometeorite identification: A magnetite rim, chondritic bulk composition, the presence of FeNi-sulfides and dehydration cracks all confirm that this particle is a micrometeorite (Genge et al., 2008). As with all micrometeorites, atmospheric entry heating has partially overprinted the particle's pre-atmospheric petrography. Dehydration cracks imply the former presence of hydrated mineralogies (i.e., generated by the loss of water from extraterrestrial phyllosilicates; Genge, 2006), similar to those found in C2 Tagish Lake, CM, CR and CI carbonaceous chondrites (Hanowski and Brearley, 2001). However, in this particle hydrated phyllosilicates have completely recrystallized, forming a metamorphic nano-crystalline, porous groundmass - as inferred from the mid-IR spectroscopic data and explained in Suttle et al., (2017a). To resolve this micrometeorite's geological history, we consider each of the main mineral assemblages or micro-textural features in turn.

Refractory minerals, anhydrous silicates and Cr-bearing spinels: Analysis of large (>4μm) relict anhydrous silicates provides clues to the parent body affinities of micrometeorites (Steele, 1992; Kurat et al., 1994; Imae et al., 2013). In CP94-050-182, three distinct populations of anhydrous silicates exist, identified by their disparate trace element contents. They include:

(1) A population of high-Ca pyroxenes (diopside) with low-Fe-Cr-enriched (LICE) [FeO/Cr_2O_5<1] and low-Fe-Mn-enriched (LIME) [FeO/MnO≈1] compositions (Fig.1C, Table.1: A3-5 [FeO/Cr_2O_3=0.4-1.1, FeO/MnO=0.6-1.4). LICE/LIME silicates are compositionally distinct from most anhydrous silicates found in carbonaceous and ordinary chondrites (Fig.7) and instead are associated with the extreme early solar system and commonly found as minor components in IDPs, Stardust samples (Dobrică et al., 2009) and refractory amoeboid aggregates (Sugiura et al., 2009). They survive as rare relicts in some chondrites (including LL3.0 Semarkona and CM2.6 Murchison, Klöck et al., 1989; Ebel et al., 2012) and have been reported in <20 individual micrometeorites among the literature (Dobrică et al., 2009; Imae, 2012).
(2) In addition, we identified a group of high-Mg pyroxene (enstatite, Table.1: A6, A7) and olivine (forsterite, Table.1: A8, A9) grains with relatively high Mn and Cr contents – similar to the LIME/LICE silicates but with significantly higher Fe concentrations (up to 19wt%) and further united by their diverse lithophile trace element contents (minor P, S, Cl and Ca [each <1wt%]). Such similar compositions suggest that these two phases share a genetic relationship as part of a single crystallization sequence.
(3) Finally, small fayalitic olivine grains (Table1: A10-A12) were also identified, containing moderate Na (<0.3wt%), S (0.2-0.3wt%) Ti (<0.3wt%) and relatively high Al (2.0-2.8wt%). Their unique and volatile-rich compositions are in stark contrast to the compositions of silicates 1 & 2.

To resolve the chronology of formation, we must consider the environmental conditions required for each population. Modelling suggests that LIME/LICE crystal compositions (Fig.1C) form by condensation at high temperatures (~1200K) and under reducing conditions from a gas of solar

composition (Ebel et al., 2012). The absence of trace Ni and Co, which readily partition into silicates under oxidising conditions, supports a reducing formation environment since these elements would otherwise partition into metal phases at low oxygen fugacities (Leroux et al., 2003). Likewise, the high Ca content (12-15wt%) implies that these crystals formed simultaneously, and in equilibrium with CAIs (Sugiura et al., 2009) from a reservoir with Ca concentrations >20wt% (Pack and Palme, 2003). Thus, the LIME/LICE silicates in CP94-050-182 are interpreted as highly refractory condensation-crystalized components, representing some of the earliest solar system solids. To preserve these crystals, they must be isolated from the nebula shortly after formation, to prevent re-equilibration at lower temperatures (Ebel et al., 2012) and also avoid re-melting whilst on the parent asteroid or during atmospheric entry. However, they are resistant to aqueous alteration (Krot et al., 2005b; Sugiura et al., 2009) and have therefore survived later parent body processing in this micrometeorite.

The condensation of LICE silicates can only occur if Cr-spinel is absent from the condensation sequence. This is because Cr preferentially partitions into oxides over silicates. As temperatures in the nebula dropped below 1200K, the onset of spinel growth would efficiently scavenged Cr from silicates (Sugiura et al., 2009). In contrast, if highly reducing conditions were maintained - for example by progressively increasing C/O ratios as oxygen condenses into silicates (Ebel and Alexander, 2005) - the condensation of spinel could be temporarily supressed. However, in CP94-050-182 both Cr-bearing anhydrous silicates and small Mn-chromite spinels (Fig.1B, Fig.3 and Table.1, A17, A18) coexist. Thus, a single equilibrium condensation sequence cannot explain the observed mineralogy. Instead, the two different Cr-bearing refractory phases are evidence of batch condensation, the addition of materials formed in distinct reservoirs (located at different distances and/or different epochs) and incorporated by large-scale radial mixing (Dobrică et al., 2012) or a later formation route for the Cr-spinels, such as by aqueous alteration.
We rule out formation by precipitation from fluids because the morphology, size and composition of aqueously generated Cr-spinel, as described in CM chondrites (Tomeoka and Buseck, 1985) is inconsistent with the characteristics of the Cr-spinels observed here in CP94-050-054. Furthermore, the Al/Cr - Fe/Mg systematics of the Cr-spinels in CP94-050-182 (Fig.8) do not provide additional clues to their formation, since they have higher Al/Cr and lower Fe/Mg ratios that either ordinary or carbonaceous chondrites. Such anomalous compositions suggest that CP94-050-052 may not be related to any known chondrite group.

After the LIME/LICE silicates, the high-Mg forsterite and enstatite population (2) would have formed under similar conditions but at lower temperatures. Although this population contains high Mn/Cr contents, this is coupled with the inclusion of volatile lithophile elements, such as P, S and Cl as well as significantly higher Fe concentrations. This strongly suggests that they formed later in the condensation sequence at lower temperatures and under rapid cooling rates (Kennedy et al., 1993). Alternatively, they could represent a second-generation of recycled silicates, formed by the reprocessing of LIME/LICE silicates in the presence of additional volatile phases, resulting in evolved Fe-rich and volatile-bearing compositions. Finally, the fayalitic olivines formed under distinctly different environmental conditions. Fayalite is associated with oxidising environments, where Fe forms Fe^{2+} cations that partition into silicates rather than metal (Ebel 2006). Within a condensation scenario this process requires unrealistically high dust enrichment factors (Fedkin & Grossman 2006). Therefore, an igneous history is more likely in which existing forsteritic olivine formed by melting, mixing and rapid recrystallization in the presence of Fe-metal and alkali-bearing glasses.

Thus, the three anhydrous silicate populations found in this micrometeorite record a complex formation history with nebula condensates preserved alongside igneous silicates and formed in at least two separate stages of volatile addition, transient melting and mixing. This is analogous to the formation histories proposed for type II chondrules - reprocessed from type I chondrules (Wasson and Rubin, 2003).

Microchondrule formation: The exceptionally small size, cryptocrystalline texture and retention of volatile alkali elements strongly suggests that the microchondrule in CP94-050-182 formed by flash heating and subsequent quenching (at >500Khr^{-1}, Bigolski et al., 2014). Likewise, the three microchondrules reported here from CM chondrites show similar sizes (with diameters <5µm, Fig.10) fine-grained textures and are either glassy or cryptocrystalline. They also share comparable bulk compositions, which are chondritic and mildly volatile enriched, with high Na concentrations of 1.2-2.2wt%. Thus, all four microchondrules likely formed by the same mechanism and under similar conditions.

Such rapid cooling rates are most easily explained by direct radiative cooling whilst residing in the cold solar nebula as free-floating objects (Bigolski et al., 2014; Dobrică and Brearley, 2013; 2016). Furthermore, the retention of volatile alkali elements requires a heating mechanism to inhibit significant evaporative loss, forcing the chondritic droplets to behave as closed systems. This can be achieved either by an extremely rapid heating cycle(s) or by maintaining dust-enriched systems, 1000's of times above solar compositions, during chondrule formation (Alexander et al., 2008). Shock waves as a viable heating source therefore seem unlikely given the prolonged pre-shock heating period associated with wave front migration (Morris et a., 2016). Likewise, vapour-melt plumes can be ruled out. Although they are capable of supporting sufficiently high dust densities to inhibit volatile (Na) evaporation, impact plumes would result in the instantaneous formation of all droplets (microchondrules and their large chondrule counterparts) whilst also producing a continuous distribution of droplet sizes. However, these features are inconsistent with the documented properties of chondrule-microchondrule aggregates which show clear evidence of repeated formation episodes and bimodal size distributions. Therefore, a different formation mechanism is required.

The close association of microchondrules with a larger "parent" chondrule provides an important constraint on their formation. In addition, because microchondrules are almost always found within the fine-grained rims of chondrules/CAIs and rarely as isolated objects in fine-grained matrix, both chondrules and microchondrules most likely formed from single, related process. Furthermore, a genetic association between chondrules and microchondrules requires that microchondrule formation is a late-stage process directly associated with chondrule recycling (Bigolski et al., 2016), rim accretion and rim metamorphism. This view is supported by Dobrică and Brearley (2013; 2016) who recently identified a subclass of microchondrules within unequilibrated ordinary chondrites that have lobate protrusions extending from their surface and connecting them directly to a parent chondrule (Fig.9 in Dobrică and Brearley, 2016). This observation, when paired with the known close compositional similarities between chondrules and microchondrules (Krot et al., 1997) suggests that microchondrules are secondary melt products directly derived from larger chondrule parents. Their formation could therefore be in collisions between chondrules as favoured by Dobrică and Brearley (2016 and Rubin et al., 1982) or by electrical discharge sheets (Bigolski et al., 2016) within an accreting mesh network (Wasson and Rubin, 2009).

The three microchondrules found in our CM chondrite samples are consistent with the above formation model, that is microchondrules in CM chondrites appear to be produced by localized melting at chondrule margins. In all instances, they are found within the fine-grained rims of chondrules (or a CAI) and have chondritic compositions close to a CI/CM bulk (Fig.5b), whilst also being distinct from ordinary chondrite compositions or microchondrules in ordinary chondrites (Fig.9). Furthermore, one of these microchondrules (Fig.10H and 10I, Fig.11) is contained within the fine-grained rim of a large compound chondrule. This object is composed of at least three plastically deformed chondrules (with diameters >200µm). Since the compound chondrule lies at the edge of the thin section, it is not fully sampled and thus could contain several more chondrules. Additionally, the fine-grained rim is thick and multi-layered, showing evidence of truncated rims surrounding only some of the host chondrules (Fig.11). This microstructure attests to a complex chronology with successive periods of chondrule formation, rim accretion, re-melting and chondrule-chondrule collisions whilst in a partially molten state. The microchondrule (Fig.10I) is included in at least the third layer of fine-

grained rim, which critically indicates formation and accretion after chondrule collisions. The outer most rim layer surrounds the entire object and includes a series of Fe-sulphide droplets representing the last phase of accretion. These simple cross-cutting relationships demonstrate the chondrule formation in Murchison (and by inference CM chondrites) involved wet chondrule collisions and microchondrule formation in a manner identical to that proposed for Semarkona by Dobrică and Brearley (2016).

In contrast to the CMs, the microchondrule in CP94-050-182 is not clearly associated with a larger chondrule parent. However, because micrometeorites are small (commonly <100µm) and rim thickness can exceed 300µm (Fig.11), as demonstrated in Murchison, it is possible that CP94-050-182 represents a subsample of fine-grained rim derived from a CM or CM-like chondrule. This suggestion is supported by the diverse assemblage of small chondritic components, the presence of an included lithic fragment with a distinctive texture (Figs.1J vs. 1K) as well as the similar compositions of the Murchison FGR and this micrometeorite's bulk matrix composition (Table.1: A22 vs. B2, Fig.5B). Thus, the textures, grain sizes and grain diversity of CP94-050-182 are consistent with the petrography of fine-grained chondrule rims and their origins are likely identical, being formed as accretionary dust mantle breccias around parent chondrules and composed of fragmented chondritic debris Rubin (1984) and Metzler et al., (1992). We therefore favour chondrule-chondrule collisions, resulting in sudden melting and shearing of droplets as the most probable formation mechanism for microchondrules.

Aqueous alteration on the parent asteroid: Most fine-grained micrometeorites are dominated by phyllosilicates, or their dehydration products (Kurat et al., 1994; Genge et al., 1997; Engrand and Maurette, 1998; Noguchi et al., 2002; Suttle et al., 2017a). They may contain accessory FeNi-sulfides (Genge et al., 2008), magnetite, carbonates (Sakamoto et al., 2010) and aqueously altered refractory objects, such as CAIs (Genge et al., 2008). To generate hydrated mineralogies such as these requires an episode of moderate-to-intense aqueous alteration; which most likely occurred whilst on the parent asteroid (Zolensky et al., 1997; Trigo-Rodríguez et al., 2006).

Currently, the average (mean or modal) degree of aqueous alteration affecting the fine-grained micrometeorite population is unknown. However, recent analysis of five giant (>400µm) Antarctic micrometeorites, whose combined surface area exceeds 2.22mm^2, revealed a complete absence of anhydrous chondrules and a paucity of anhydrous silicates (Suttle et al., 2018). Likewise, previous analyses of small fine-grained Antarctic micrometeorites have identified an apparent deficit of chondrules derived from C2 parent bodies (Engrand and Maurette, 1998; Varela and Kurat, 2009 (and references therein); Reshma et al., 2013), as well as evidence for intense aqueous alteration (Noguchi et al., 2002; Sakamoto et al., 2010; Suttle et al., 2017b). Furthermore, the flux of coarse-grained micrometeorites, which largely represent fragmented chondrules (Genge et al., 2005; van Ginneken et al., 2012), are primarily related to ordinary chondrite precursors (~70%), although intact anhydrous chondrule material from CM chondrite precursors has been recognised (Genge et al., 2005; van Ginneken et al., 2012). Collectively, this body of evidence suggests that most micrometeorites experienced at least moderate aqueous alteration, while a large proportion of the population record episodes of intense alteration - equivalent to the CM1 petrologic subtype and resulting in the complete secondary replacement of anhydrous chondrules (Suttle et al., 2018).

In CP94-050-182, the matrix was primarily composed of phyllosilicates, now recrystalized to olivine (as explained previously and in Suttle et al., 2017a). Likewise, many of the anhydrous phases show clear evidence of significant replacement and alteration. Elemental mapping identified a triangular-shaped region containing elevated concentrations of Ca, Al and Ti (Fig.2D, 1E and 1H). Such dense clustering of refractory elements implies the presence of a small CAI (Fig.1F, Table.1: A13-A16). However, this Ca-Al-Ti hotspot is poorly preserved, with a skeletal appearance and is intermixed with fine-grained matrix. These properties suggest that the CAI has experienced extensive alteration and now closely resembles previously described ghost CAIs in CM chondrites and micrometeorites (Greenwood et al., 1994; Genge et al., 2008).

Similarly, all three populations of anhydrous silicate in this micrometeorite have anhedral morphologies, some with rounded shaped and all are mantled by a coarse non-stochiometric Fe-rich phase (Fig.1C-F & 1I). This texture is common in CM chondrites and fine-grained micrometeorites affected by advanced aqueous alteration (Tomeoka and Busek, 1985; Hanowski and Brearley, 2001; Suttle et al., 2018) and reflects the growth secondary hydrated phases such as coarse-grained cronstedtite (Greenwood et al., 1994), ferrihydrite and Fe-sulfides (Genge et al., 2008). Notably, the LICE silicates have multiple, penetrating, micron-scale irregular cracks, which are either empty or infilled with a material of higher atomic weight. These features are similar to the meshwork replacement textures described in CM Nogoya by Velbel et al., (2012) [Figs.3 & 4] and the serpentine veining features described by Lee and Lindgren, (2016) from the CM2.6 Murchison meteorite. Collectively these observations suggests that the anhydrous silicates initially acted as a substrate and later as a donor phase for alteration. However, because micrometeorites are affected by atmospheric entry heating, the hydrated alteration phases experienced thermal decomposition and are no longer preserved, instead, showing a mixed assemblage of Fe-oxides (Greshake et al., 1998; Toppani et al., 2001).

Further evidence for aqueous alteration is seen in the microchondrule's texture and geochemical zonation. This object would have initially formed as an igneous glass by quench cooling and subsequently devitrified, forming the nano-crystalline texture (Fig.3). Thus, the original glass would have been homogenous and only later, during aqueous alteration and solid-state diffusion could the observed geochemical heterogeneities be generated (Fig.3). The presence of a S-bearing rim surrounding the microchondrule likewise implies that S – a highly fluid-mobile element – was leached from the glass after formation and re-precipitated locally as an alteration deposit around the microchondrule as a thin rim (Fig.3B). The leaching of chondrule glasses during aqueous alteration is common in CR2 and CM2 chondrites and can result in depletions of Ni, S, P and alkali elements [Na and K] (Hanowski and Brearley, 2001). Furthermore, near-identical zonation is observed in all three microchondrules from the CM chondrites. They are in two different meteorites and in all instances show the same alteration features, including the formation of poorly crystalline phyllosilicate (Fig.10G) and localized leaching of material (Fig.10E). This provides clear evidence for (incomplete) alteration. We can rule out terrestrial alteration since these features are observed in the microchondrules from Murchison (an observed fall, not significantly affected by terrestrial weathering) as well as in EET 96029 and CP94-050-182 that have some terrestrial weathering effects (Lee et al., 2016). However, aqueous alteration in this micrometeorite was incomplete and potentially short duration, as demonstrated by the retention of some large (>4μm) anhydrous silicates, the preservation of primitive silicate compositions and incomplete alteration of the microchondrule.

Implications

The parent body affinities of CP94-050-182: This micrometeorite preserves evidence for a complex history with each of the main components generated by different events and at different times. In this study, we demonstrated that it is possible to reconstruct the geological history of unmelted micrometeorites, where each stage in the particle's history is only partially overprinted by subsequent processes. This micrometeorite provides evidence for radial mixing or batch condensation crystallization in the solar nebula as well as a complex accretionary history. The latter requires multiple stages of growth and disruption resulting in the presence of the included lithic clast as well as the small sizes of (a disintegrated) CAI and fragmented anhydrous silicates. Later, whilst on the parent body, aqueous alteration produced the phyllosilicate-rich matrix and Fe-rich mantles surrounding the refractory components. Finally, the micrometeorite experienced modest flash heating during atmospheric entry and mild terrestrial alteration whilst stored in Antarctic ice. This later terrestrial heating and alteration being similar to the moderate thermal metamorphism and Antarctic weathering experienced by EET 96029 (Lee et al., 2016) although showing no noticeable effect of the microchondrule's composition or texture.

584 We interpret this particle as a fragment of fine-grained rim that once surrounded a larger parent
585 chondrule. A CM or CM-like parent body seems most likely given notable similarities with this
586 meteorite class in terms of bulk matrix compositions, microchondrule properties and aqueous
587 alteration histories. However, it is also possible that this micrometeorite was derived from a different
588 source, currently unrepresented by meteorite collections. This suggestion is supported by the
589 presence of Cr-spinels with unique compositions (Fig.8) distinct from carbonaceous chondrites, as well
590 as LIME/LICE silicates which are otherwise rare in carbonaceous chondrites. Thus, a cometary parent
591 body is another possible source, as they also contain LIME/LICE silicates, microchondrules (Noguchi et
592 al., 2017), and minerals with exotic or extreme chemical compositions.

593 ## Conclusions

594 We investigated a single fine-grained unmelted Antarctic micrometeorite with a hydrated, chondritic
595 and Cr-rich mineralogy. This particle contains a diverse mineral assemblage with multiple features of
596 interest, most notably a cryptocrystalline microchondrule with a geochemical zoning (revealing a
597 distinct core, margin and rim). We compare this object against three newly described microchondrules
598 from CM chondrites. Collectively these four objects represent the first detailed petrographic data for
599 microchondrules in a hydrated chondritic host, and thus further demonstrate the ubiquity of
600 microchondrules in chondritic meteorites. Microchondrule formation appears to be intimately
601 associated with the accretion of fine-grained rims on larger chondrule parents and with their later
602 modification by flash heating. We agree with the previous conclusions of Dobrică and Brearley (2016)
603 that microchondrules are most likely generated in chondrule collisions where melt droplets at the
604 chondrule margin escape their parent chondrule. However, these droplets must then rapidly cool and
605 cannot travel far before they are again trapped during the accretion of fine-grained rims. The entire
606 chondrule and rim formation mechanism was cyclic, high-energy, rapid and occurred in high density
607 environments rich in fragmented refractory materials and lithic clasts.

608 ## Acknowledgements

609 The data presented in this paper were acquired primarily during Martin Suttle's PhD research whilst at Imperial
610 College London and the NHM and principally funded by the Science and Technology Council (STFC) under a
611 training grant (ST/M503526/1). However, research continued whilst Martin Suttle attended a post-doc research
612 position at the University of Pisa, which is funded through two Italian research grants MIUR: PNRA16_00029
613 [Programma Nazionale delle Ricerche in Antartide – CUP I52F17001050005] and PRIN2015_20158W4JZ7 [CUP
614 I52F15000310001 for the "Meteoriti Antartiche"]. Lugi Folco is also supported through the same research grants,
615 while Matthew Genge and Sara Russell are funded by the STFC (ST/J001260/1 and ST/M00094X/1 respectively)
616 and Martin Lee is funded by STFC grants (ST/N000846/1 and ST/H002960/1). We thank John Spratt and Tomasz
617 Góral at the NHM, London and Tina Geriaki at Diamond Lightsource for their support and advice during and
618 analytical acquisition. Further, we thank NASA ANSMET for the loan of EET 96029. We also thank two anonymous
619 reviewers for their time spent on this manuscript and likewise our associate editor Don Brownlee.

620 ## References

621 Alexander, C.O.D., Grossman, J.N., Ebel, D.S. and Ciesla, F.J., 2008. The formation conditions of chondrules and
622 chondrites. *Science*, 320:1617-1619, doi:10.1126/science.1156561.

623 Bigolski, J.N., Weisberg, M.K., Ebel, D.S. and Connolly, H.C., 2014. Microchondrules: Records of multiple heating
624 events in the solar nebula and implications for type II chondrule formation. 45th Annual Lunar and Planetary
625 Science Conference, held 17-21th March, 2014, The Woodlands Convention, Texas, USA (abstract #1879).

626 Bigolski, J.N., Weisberg, M.K., Connolly, H.C. and Ebel, D.S., 2016. Microchondrules in three unequilibrated
627 ordinary chondrites. *Meteoritics & Planetary Science*, 51:235-260, doi:10.1111/maps.12585.

628 Brearley A. J. and Jones R. H. 1998. Chondritic meteorites. In Planetary Materials (ed. P. H. Ribbe). Reviews in
629 Mineralogy 36:313-398.

630 Bright, D.S. and Newbury, D.E., 2004. Maximum pixel spectrum: a new tool for detecting and recovering rare,
631 unanticipated features from spectrum image data cubes. *Journal of microscopy*, 216:186-193,
632 doi:10.1111/j.0022-2720.2004.01412.x.

633 Bunch, T.E., Keil, K. and Snetsinger, K.G., 1967. Chromite composition in relation to chemistry and texture of
634 ordinary chondrites. *Geochimica et Cosmochimica Acta*, 31:1569-1582, doi:10.1016/0016-7037(67)90105-6.

635 Burgess, S., Li, X. and Holland, J., 2013. High spatial resolution energy dispersive X-ray spectrometry in the SEM
636 and the detection of light elements including lithium. *Microscopy and Analysis*, 6:S8-S13.

637 Cordier, C., Baecker, B., Ott, U., Folco, L. and Trieloff, M., 2018. A new type of oxidized and pre-irradiated
638 micrometeorite. *Geochimica et Cosmochimica Acta*, 233:135-158, doi:10.1016/j.gca.2018.04.010.

639 Dalton, J.A. and Lane, S.J., 1996. Electron microprobe analysis of Ca in olivine close to grain boundaries: the
640 problem of secondary X-ray fluorescence. *American Mineralogist*, 81:194-201, doi:10.2138/am-1996-1-224.

641 Dartois, E., Engrand, C., Brunetto, R., Duprat, J., Pino, T., Quirico, E., Remusat, L., Bardin, N., Briani, G.,
642 Mostefaoui, S. and Morinaud, G., 2013. UltraCarbonaceous Antarctic micrometeorites, probing the Solar System
643 beyond the nitrogen snow-line. *Icarus*, 224:243-252, doi:10.1016/j.icarus.2013.03.002.

644 Dartois, E., Engrand, C., Duprat, J., Godard, M., Charon, E., Delauche, L., Sandt, C. and Borondics, F., 2018. Dome
645 C ultracarbonaceous Antarctic micrometeorites-Infrared and Raman fingerprints. *Astronomy & Astrophysics*,
646 609:A65-73, doi:10.1051/0004-6361/201731322.

647 Dobrică, E., Engrand, C., Duprat, J., Gounelle, M., Leroux, H., Quirico, E. and Rouzaud, J.N., 2009. Connection
648 between micrometeorites and Wild 2 particles: From Antarctic snow to cometary ices. *Meteoritics & Planetary*
649 *Science*, 44:1643-1661, doi:10.1111/j.1945-5100.2009.tb01196.

650 Dobrică, E. and Brearley, A.J., 2013. Ubiquitous microchondrules in the matrix of unequilibrated ordinary
651 chondrites. 44th Lunar and Planetary Science Conference, held 18-22nd March, 2013. The Woodlands Convention,
652 Texas, USA. (abstract #2701).

653 Dobrică, E. and Brearley, A.J., 2016. Microchondrules in two unequilibrated ordinary chondrites: Evidence for
654 formation by splattering from chondrules during stochastic collisions in the solar nebula. *Meteoritics & Planetary*
655 *Science*, 51:884-905, doi:10.1111/maps.12633.

656 Dobrică, E., Le Guillou, C. and Brearley, A.J., 2018. Aqueous Alteration of Porous Microchondrules in Semarkona:
657 Implications for Hydration, Oxidation and Elemental Exchange Processes. *Geochimica et Cosmochimica Acta*,
658 doi:.10.1016/j.gca.2018.10.002

659 Dodd, R.T., 1978. Compositions of droplet chondrules in the Manych (L-3) chondrite and the origin of chondrules.
660 *Earth and Planetary Science Letters*, 40:71-82, doi:10.1016/0012-821X(78)90075-4.

661 Duprat, J., Dobrică, E., Engrand, C., Aléon, J., Marrocchi, Y., Mostefaoui, S., Meibom, A., Leroux, H., Rouzaud,
662 J.N., Gounelle, M. and Robert, F., 2010. Extreme deuterium excesses in ultracarbonaceous micrometeorites from
663 central Antarctic snow. *Science*, 328:742-745, doi:10.1126/science.1184832.

664 Drouin, D., Couture, A.R., Joly, D., Tastet, X., Aimez, V. and Gauvin, R., 2007. CASINO V2. 42—A Fast and Easy-to-
665 use Modelling Tool for Scanning Electron Microscopy and Microanalysis Users. *Scanning*, 29:92-101,
666 doi:10.1002/sca.20000.

667 Ebel, D.S. and Alexander, C.M., 2005. Condensation from cluster-IDP enriched vapor inside the snow line:
668 Implications for Mercury, asteroids, and enstatite chondrites. 36th Annual Lunar and Planetary Science
669 Conference, held 14-18th March, 2005, The Woodlands Convention, Texas, USA (abstract #1797).

670 Ebel, D.S., Weisberg, M.K. and Beckett, J.R., 2012. Thermochemical stability of low-iron, manganese-enriched
671 olivine in astrophysical environments. *Meteoritics & Planetary Science*, 47:585-593, doi:10.1111/j.1945-
672 5100.2012.01347.x.

673 Engrand, C. and Maurette, M., 1998. Carbonaceous micrometeorites from Antarctica. *Meteoritics & Planetary*
674 *Science*, 33:565-580, doi:10.1111/j.1945-5100.1998.tb01665.x.

675 Farinella, P., Gonczi, R., Froeschlé, C. and Froeschlé, C., 1993. The injection of asteroid fragments into
676 resonances. *Icarus*, 101:174-187, doi:10.1006/icar.1993.1016.

677 Fruland, R.M., King, E.A. and McKay, D.S., 1978. Allende dark inclusions. In Lunar and Planetary Science
678 Conference Proceedings (Vol. 9, pp. 1305-1329). 9th Annual Lunar and Planetary Science Conference, held 13-
679 17th March, 1978, The Woodlands Convention, Texas, USA (1:1305-1329).

680 Fudali, R.F. and Noonan, A.F., 1975. Gobabeb, a new chondrite: The coexistence of equilibrated silicates and
681 unequilibrated spinels. Meteoritics & Planetary Science, 10:31-39, doi:10.1111/j.1945-5100.1975.tb00005.x.

682 Genge, M.J., 2006. Igneous rims on micrometeorites: *Geochimica et Cosmochimica Acta*, 70:2603-2621,
683 doi:10.1016/j.gca.2006.02.005.

684 Genge, M.J., 2008. Koronis asteroid dust within Antarctic ice. Geology, 36:687-690, doi:10.1130/G24493A.1.

685 Genge, M.J., Grady, M.M. and Hutchison, R., 1997. The textures and compositions of fine-grained Antarctic
686 micrometeorites: Implications for comparisons with meteorites. *Geochimica et Cosmochimica Acta*, 61:5149-
687 5162, doi:10.1016/S0016-7037(97)00308-6.

688 Genge, M.J., Gileski, A. and Grady, M.M., 2005. Chondrules in Antarctic micrometeorites. *Meteoritics &*
689 *Planetary Science*, 40:225-238, doi:10.1111/j.1945-5100.2005.tb00377.x.

690 Genge, M.J., Engrand, C., Gounelle, M. and Taylor, S., 2008. The classification of micrometeorites. *Meteoritics &*
691 *Planetary Science*, 43:497-515, doi:10.1111/j.1945-5100.2008.tb00668.x.

692 Gonczi, R., Froeschlé, C. and Froeschlé, C., 1982. Poynting-Robertson drag and orbital resonance. Icarus, 51:633-
693 654, doi:10.1016/0019-1035(82)90152-X.

694 Gounelle, M., Chaussidon, M., Morbidelli, A., Barrat, J.A., Engrand, C., Zolensky, M.E. and McKeegan, K.D., 2009.
695 A unique basaltic micrometeorite expands the inventory of solar system planetary crusts. *Proceedings of the*
696 *National Academy of Sciences*, 106:6904-6909, doi:10.1073?pnas.0900328106.

697 Greenwood, R.C., Lee, M.R., Hutchison, R. and Barber, D.J., 1994. Formation and alteration of CAIs in Cold
698 Bokkeveld (CM2). *Geochimica et Cosmochimica Acta*, 58:1913-1935, doi:10.1016/0016-7037(94)90424-3.

699 Greenwood, R.C., Burbine, T.H., Miller, M.F. and Franchi, I.A., 2017. Melting and differentiation of early-formed
700 asteroids: The perspective from high precision oxygen isotope studies. *Chemie der Erde*, 77:1-43,
701 doi:10.1016/j.chemer.2016.09.005.

702 Hanowski, N.P. and Brearley, A.J., 2001. Aqueous alteration of chondrules in the CM carbonaceous chondrite,
703 Allan Hills 81002: Implications for parent body alteration. *Geochimica et Cosmochimica Acta*, 65:495-518,
704 doi:10.1016/S0016-7037(00)00552-4.

705 Hewins, R.H., 1997. Chondrules. Annual Review of Earth and Planetary Sciences, 25:61-83,
706 doi:10.1146/annurev.earth.25.1.61.

707 Imae, N., 2012. Cometary dust in Antarctic micrometeorites. *Proceedings of the International Astronomical*
708 *Union*, 8:123-129, doi:10.1017/S1743921312016766.

709 Imae, N., Taylor, S. and Iwata, N., 2013. Micrometeorite precursors: Clues from the mineralogy and petrology of
710 their relict minerals. *Geochimica et Cosmochimica Acta*, 100:116-157, doi:10.1016/j.gca.2012.09.052.

711 Johnson, C.A. and Prinz, M., 1991. Chromite and olivine in type II chondrules in carbonaceous and ordinary
712 chondrites: Implications for thermal histories and group differences. *Geochimica et Cosmochimica Acta*, 55: 893-
713 904, doi:10.1016/0016-7037(91)90349-A.

714 Klöck, W., Thomas, K.L., McKay, D.S. and Palme, H., 1989. Unusual olivine and pyroxene composition in
715 interplanetary dust and unequilibrated ordinary chondrites. *Nature*, 339:126-128, doi:10.1038/339126a0.

716 Krot, A.N. and Rubin, A.E., 1996. Microchondrule-bearing chondrule rims: constraints on chondrule formation.
717 Chapter 9 (181-184) in: Chondrules and the protoplanetary disk (ed. RH Hewins, RH Jones Sz ERD Scott), ISBN-
718 13:9780521552882, Cambridge, UK: Cambridge University Press, 2011.

719 Krot, A.N., Rubin, A.E., Keil, K. and Wasson, J.T., 1997. Microchondrules in ordinary chondrites: Implications for
720 chondrule formation. *Geochimica et Cosmochimica Acta*, 61:463-473, doi:10.1016/S0016-7037(96)00342-0.

721 Krot, A.N., Amelin, Y., Cassen, P. and Meibom, A., 2005a. Young chondrules in CB chondrites from a giant impact
722 in the early solar system. *Nature*, 436:989-992, doi:10.1038/nature03830.

723 Krot, A.N., Fagan, T.J., Nagashima, K., Petaev, M.I. and Yurimoto, H., 2005b. Origin of low-Ca pyroxene in
724 amoeboid olivine aggregates: Evidence from oxygen isotopic compositions. *Geochimica et cosmochimica acta*,
725 69:1873-1881, doi:10.1016/j.gca.2004.06.046.

726 Krot, A.N., Ivanova, M.A. and Ulyanov, A.A., 2007. Chondrules in the CB/CH-like carbonaceous chondrite
727 Isheyevo: Evidence for various chondrule-forming mechanisms and multiple chondrule generations. *Chemie der*
728 *Erde-Geochemistry*, 67:283-300, doi:10.1016/j.chemer.2006.04.001.

729 Kurat, G., Koeberl, C., Presper, T., Brandstätter, F. and Maurette, M., 1994. Petrology and geochemistry of
730 Antarctic micrometeorites. *Geochimica et Cosmochimica Acta*, 58:3879-3904, doi:10.1016/0016-
731 7037(94)90369-7.

732 Lee, M.R., Lindgren, P., King, A.J., Greenwood, R.C., Franchi, I.A. and Sparkes, R., 2016. Elephant Moraine 96029,
733 a very mildly aqueously altered and heated CM carbonaceous chondrite: Implications for the drivers of parent
734 body processing. *Geochimica et Cosmochimica Acta*, 187:237-259, doi:10.1016/j.gca.2016.05.008.

735 Leroux, H., Libourel, G., Lemelle, L. and Guyot, F., 2003. Experimental study and TEM characterization of dusty
736 olivines in chondrites: Evidence for formation by in situ reduction. *Meteoritics & Planetary Science*, 38:81-94,
737 doi:10.1111/j.1945-5100.2003.tb01047.x.

738 Llovet, X., Pinard, P.T., Donovan, J.J. and Salvat, F., 2012. Secondary fluorescence in electron probe microanalysis
739 of material couples. *Journal of Physics D: Applied Physics*, 45:225301, doi:10.1088/0022-3727/45/22/225301.

740 Lodders, K., 2003. Solar system abundances and condensation temperatures of the elements. *The Astrophysical*
741 *Journa*l, 591:1220-1247, doi:10.1086/375492.

742 Maurette, M., Olinger, C., Michel-Levy, M.C., Kurat, G., Pourchet, M., Brandstätter, F. and Bourot-Denise, M.,
743 1991. A collection of diverse micrometeorites recovered from 100 tonnes of Antarctic blue ice. *Nature*, 351:44-
744 46, doi:10.1038/351044a0.

745 Merlet, C. and Llovet, X., 2012. Uncertainty and capability of quantitative EPMA at low voltage–A review. In IOP
746 Conference Series: *Materials Science and Engineering*, 32:1-15, doi:10.1088/1757-899X/32/1/012016.

747 Metzler, K., Bischoff, A. and Stöffler, D., 1992. Accretionary dust mantles in CM chondrites: Evidence for solar
748 nebula processes. *Geochimica et Cosmochimica Acta*, 56:2873-2897, doi:10.1016/0016-7037(92)90365-P.

749 Morgan, G.B. and London, D., 1996. Optimizing the electron microprobe analysis of hydrous alkali
750 aluminosilicate glasses. *American Mineralogist*, 81:1176-1185, doi:10.2138/am-1996-9-1016.

751 Morgan, G.B. and London, D., 2005. Effect of current density on the electron microprobe analysis of alkali
752 aluminosilicate glasses. *American Mineralogist*, 90:1131-1138, doi:10.2138/am.2005.1769.

753 Morris, M.A., Weidenschilling, S.J. and Desch, S.J., 2016. The effect of multiple particle sizes on cooling rates of
754 chondrules produced in large-scale shocks in the solar nebula. *Meteoritics & Planetary Science*, 51:870-883,
755 doi:10.1111/maps.12631-2309.

756 Nesvorný, D., Vokrouhlický, D., Bottke, W.F. and Sykes, M., 2006. Physical properties of asteroid dust bands and
757 their sources. *Icarus*, 181:107-144, doi:10.1016/j.icarus.2005.10.022.

758 Noguchi, T., Nakamura, T. and Nozaki, W., 2002. Mineralogy of phyllosilicate-rich micrometeorites and
759 comparison with Tagish Lake and Sayama meteorites. *Earth and Planetary Science Letters*, 202:229-246,
760 doi:10.1016/S0016-7037(01)00722-0.

761 Noguchi, T., Tsujimoto, S., Okazaki, R., Nakamura, T., Ebihara, M., Ito, S., Nagahara, H., Tachibana, S., Terada, K.
762 and Yabuta, H., 2013. A Fine-Grained Polycrystalline Micrometeorite: An Asteroidal Dust Particle with a Unique
763 Mineralogy. 76th Annual meeting of the Meteoritical Society, held 29 July – 2 August, 2013 in RASC Edmonton
764 Centre, Alberta, Canada. (abstract #5981)

765 Noguchi, T., Yabuta, H., Itoh, S., Sakamoto, N., Mitsunari, T., Okubo, A., Okazaki, R., Nakamura, T., Tachibana, S.,
766 Terada, K. and Ebihara, M., 2017. Variation of mineralogy and organic material during the early stages of aqueous
767 activity recorded in Antarctic micrometeorites. *Geochimica et Cosmochimica Acta*, 208:119-144,
768 doi:10.1016/j.gca.2017.03.034.

769 Pack, A. and Palme, H., 2003. Partitioning of Ca and Al between forsterite and silicate melt in dynamic systems
770 with implications for the origin of Ca, Al-rich forsterites in primitive meteorites. *Meteoritics & Planetary Science*,
771 38:1263-1281, doi:10.1111/j.1945-5100.2003.tb00312.x.

772 Pinard, P.T., Terborg, R., Salge, T. and Richter, S., 2015. Evaluation of Combined Quantification of Cr-Ni Steel
773 using EDS and WDS. *Microscopy and Microanalysis*, 21:1879-1880, doi:10.1017/S143192761501017X.

774 Rubin, A.E., Scott, E.R. and Keil, K., 1982. Microchondrule-bearing clast in the Piancaldoli LL3 meteorite: a new
775 kind of type 3 chondrite and its relevance to the history of chondrules. *Geochimica et Cosmochimica Acta*,
776 46:1763-1776, doi:10.1016/0016-7037(82)90116-8.

777 Rubin, A.E., 1984. Coarse-grained chondrule rims in type 3 chondrites. *Geochimica et Cosmochimica Acta*,
778 48:1779-1789, doi:10.1016/0016-7037(84)90032-2.

779 Rubin, A.E. and Grossman, J.N., 2010. Meteorite and meteoroid: New comprehensive definitions. *Meteoritics &*
780 *Planetary Science*, 45:114-122, doi:10.1111/j.1945-5100.2009.01009.x.

781 Sakamoto, K., Nakamura, T., Noguchi, T. and Tsuchiyama, A., 2010. A new variant of saponite-rich
782 micrometeorites recovered from recent Antarctic snowfall. *Meteoritics & Planetary Science*, 45:220-237,
783 doi:10.1111/j.1945-5100.2010.01019.x.

784 Salge T., Krzesinska, A. and Mohr-Westheide, T. 2017. Non-destructive imaging of Martian meteorite Chassigny
785 and quantification of platinum group metals from archean spherule layers in the Baberton Greenstone Belt,
786 South Africa using low voltage FEG SEM/EDS. 80th Annual Meeting of the Meteoritical Society, held July 23-28,
787 2017 in Santa Fe, New Mexico. (abstract #6209).

788 Suavet, C., Alexandre, A., Franchi, I.A., Gattacceca, J., Sonzogni, C., Greenwood, R.C., Folco, L. and Rochette, P.,
789 2010. Identification of the parent bodies of micrometeorites with high-precision oxygen isotope ratios. *Earth*
790 *and Planetary Science Letters*, 293:313-320, doi:10.1016/j.epsl.2010.02.046.

791 Sugiura, N., Petaev, M.I., Kimura, M., Miyazaki, A. and Hiyagon, H., 2009. Nebular history of amoeboid olivine
792 aggregates. *Meteoritics & Planetary Science*, 44:559-572, doi:10.1111/j.1945-5100.2009.tb00751.x.

793 Steele, I.M., 1992. Olivine in Antarctic micrometeorites: Comparison with other extraterrestrial olivine.
794 *Geochimica et Cosmochimica Acta*, 56:2923-2929, doi:10.1016/0016-7037(92)90368-S.

795 Suttle, M.D., Genge, M.J., Folco, L. and Russell, S.S., 2017a. The thermal decomposition of fine-grained
796 micrometeorites, observations from mid-IR spectroscopy. *Geochimica et Cosmochimica Acta*, 206:112-136,
797 doi:10.1016/j.gca.2017.03.002.

798 Suttle, M.D., Genge, M.J. and Russell, S.S., 2017b. Shock fabrics in fine-grained micrometeorites. *Meteoritics &*
799 *Planetary Science*, 52:2258–2274, doi:10.1111/maps.12927

800 Suttle, M.D., Genge, M.J., Folco, L., Lin, Q., Russell, S.S., and Najorka, J. 2018. Intense aqueous alteration in giant
801 fine-grained micrometeorites *Geochimica et Cosmochimica Acta*, *submitted*.

802 Taylor, S., Matrajt, G. and Guan, Y., 2012. Fine-grained precursors dominate the micrometeorite flux. *Meteoritics*
803 *& Planetary Science*, 47:550-564, doi:10.1111/j.1945-5100.2011.01292.x.

804 Trigo-Rodriguez, J.M., Rubin, A.E. and Wasson, J.T., 2006. Non-nebular origin of dark mantles around chondrules
805 and inclusions in CM chondrites. *Geochimica et Cosmochimica Acta*, 70:1271-1290,
806 doi:10.1016/j.gca.2005.11.009.

807 Tomeoka, K. and Buseck, P.R., 1985. Indicators of aqueous alteration in CM carbonaceous chondrites:
808 Microtextures of a layered mineral containing Fe, S, O and Ni. *Geochimica et Cosmochimica Acta*, 49:2149-2163,
809 doi:10.1016/0016-7037(85)90073-0.

810 Toppani, A., Libourel, G., Engrand, C. and Maurette, M., 2001. Experimental simulation of atmospheric entry of
811 micrometeorites. *Meteoritics & Planetary Science*, 36:1377-1396, doi:10.1111/j.1945-5100.2001.tb01831.x.

812 van Ginneken, M., Folco, L., Cordier, C. and Rochette, P., 2012. Chondritic micrometeorites from the
813 Transantarctic Mountains. *Meteoritics & Planetary Science*, 47:228-247, doi:10.1111/j.1945-5100.2011.01322.x.

814 van Ginneken, M., Gattacceca, J., Rochette, P., Sonzogni, C., Alexandre, A., Vidal, V. and Genge, M.J., 2017. The
815 parent body controls on cosmic spherule texture: Evidence from the oxygen isotopic compositions of large
816 micrometeorites. *Geochimica et Cosmochimica Acta*, 212:196-210, doi:10.1016/j.gca.2017.05.008.

817 Varela, M.E., Kurat, G. and Zinner, E., 2005. A liquid-supported condensation of major minerals in the solar
818 nebula: evidence from glasses in the Kaba (CV3) chondrite. *Icarus*, 178:553-569,
819 doi:10.1016/j.icarus.2005.05.001.

820 Velbel, M.A., Tonui, E.K. and Zolensky, M.E., 2012. Replacement of olivine by serpentine in the carbonaceous
821 chondrite Nogoya (CM2). *Geochimica et Cosmochimica Acta*, 87:117-135, doi:10.1016/j.gca.2012.03.016.

822 Vokrouhlický, D. and Farinella, P., 2000. Efficient delivery of meteorites to the Earth from a wide range of
823 asteroid parent bodies. *Nature*, 407:606-608, doi:10.1038/35036528.

824 Vokrouhlický, D., Nesvorný, D. and Bottke, W.F., 2008. Evolution of dust trails into bands. *The Astrophysical*
825 *Journal*, 672:696-712.

826 Wasson, J.T., 1993. Constraints on chondrule origins. Meteoritics & Planetary Science, 28:14-28,
827 doi:10.1111/j.1945-5100.1993.tb00244.x.

828 Wasson, J.T., Krot, A.N., Lee, M.S. and Rubin, A.E., 1995. Compound chondrules. *Geochimica et Cosmochimica*
829 *Acta*, 59:1847-1869, doi:10.1016/0016-7037(95)00087-G.

830 Wasson, J.T. and Rubin, A.E., 2003. Ubiquitous low-FeO relict grains in type II chondrules and limited
831 overgrowths on phenocrysts following the final melting event. *Geochimica et Cosmochimica Acta*, 67:2239-2250,
832 doi:10.1016/S0016-7037(03)00023-1

833 Wasson, J.T. and Rubin, A.E., 2009. Composition of matrix in the CR chondrite LAP 02342. *Geochimica et*
834 *Cosmochimica Acta*, 73:1436-1460, doi:10.1016/j.gca.2008.11.044.

835 Weisberg, M.K., Prinz, M., Clayton, R.N. and Mayeda, T.K., 1993. The CR (Renazzo-type) carbonaceous chondrite
836 group and its implications. *Geochimica et Cosmochimica Acta*, 57:1567-1586, doi:10.1016/0016-7037(93)90013-
837 M.

838 Wendt, M. and Schmidt, A., 1978. Improved reproducibility of energy-dispersive X-ray microanalysis by
839 normalization to the background. physica status solidi 46:179-183, doi:10.1002/pssa.2210460121.

840 Wlotzka F. 2005. Cr spinel and chromite as petrogenetic indicators in ordinary chondrites: Equilibration
841 temperatures of petrologic types 3.7 to 6. *Meteoritics & Planetary Science* 40:1673–1702, doi:10.1111/j.1945-
842 5100.2005.tb00138.x.

843 Wyatt, S.P. and Whipple, F.L., 1950. The Poynting-Robertson effect on meteor orbits. *The Astrophysical Journal*,
844 111:134-141.

845 Yabuta, H., Noguchi, T., Itoh, S., Nakamura, T., Miyake, A., Tsujimoto, S., Ohashi, N., Sakamoto, N., Hashiguchi,
846 M., Abe, K.I. and Okubo, A., 2017. Formation of an ultracarbonaceous Antarctic micrometeorite through minimal
847 aqueous alteration in a small porous icy body. *Geochimica et Cosmochimica Acta*, 214:172-190,
848 doi:10.1016/j.gca.2017.06.047.

849 Zolensky, M.E., Mittlefehldt, D.W., Lipschutz, M.E., Wang, M.S., Clayton, R.N., Mayeda, T.K., Grady, M.M.,
850 Pillinger, C. and David, B., 1997. CM chondrites exhibit the complete petrologic range from type 2 to 1.
851 *Geochimica et Cosmochimica Acta*, 61:5099-5115, doi:10.1016/S0016-7037(97)00357-8.

852 Zolensky, M., Nakamura-Messenger, K., Rietmeijer, F., Leroux, H., Mikouchi, T., Ohsumi, K., Simon, S.,
853 Grossman, L., Stephan, T., Weisberg, M. and Velbel, M., 2008. Comparing Wild 2 particles to chondrites and
854 IDPs. *Meteoritics & Planetary Science*, 43:261-272, doi:10.1111/j.1945-5100.2008.tb00621.x.

855

List of figures and tables

Table.1. SEM-EDS analyses of various phases within CP94-050-182 (A1-A22), as well as microchondrule and fine-grained matrix in CM Murchison (B1 & B2). Values are listed in weight percent, quoted to 1 decimal place and their suspected phases listed. We also show their At% stochiometric ratios for several elements and calculated Mg#, which aid in the identification and characterisation of mineralogy. Analyses were collected using either standards-based EDS (marked as EVO) or as standardless EDS extracted from the hyperspectral imaging dataset or collected as direct spot analyses (and marked as FEI 650 or 450 respectively). The standardless EDS FEI 650 results have their displayed weight totals normalized to 100wt% [*italicized*]. (Note: "-" represents values for below analytical detection limits, additionally, the uncorrected weight totals, displayed for the EVO analyses, which exceed 100wt% [A3, A4] suggest an inhomogeneous sample volume and therefore beam overlap).

ID	Instrument	No.	Na	Mg	Al	Si	P	S	Cl	K	Ca	Ti	Cr	Mn	Fe	Ni	Zn	O	Total	At% O/Si	At% O/Fe	At% Mg#	Suspected phase	Solid solution composition	Notes
A1	EVO	3	1.9	9.8	1.5	16.1	-	0.3	1.2	0.5	0.8	-	0.5	0.2	18.8	-	0.1	33.3	85.0	3.6	6.2	54	Amorphous after phyllosilicate	-	Atered microchondrule
A2	FEI 650	-	0.4	9.5	1.7	19.9	-	0.2	0.1	0.1	0.8	-	0.6	-	17.8	-	-	37.0	88.0	3.3	7.3	55			
A3	EVO	1	-	12.5	2.1	26.2	-	-	-	-	14.9	0.5	1.4	0.8	0.9	-	-	47.3	106.6	3.2	175.8	97	High-Ca Pyroxene	En57, Fs2, Wo41	LICE pyroxenes [Diopside]
A4	EVO	1	-	12.3	2.9	25.0	-	-	0.2	-	12.4	0.4	1.4	1.7	2.4	-	-	46.2	104.8	3.2	68.1	92	FeO/MnO=0.6-1.4	En59, Fs5, Wo36	
A5	*FEI 450*	*2*	*0.1*	*13.2*	*2.7*	*26.8*	-	*0.1*	-	-	*17.5*	*0.5*	*1.4*	*1.3*	*0.8*	-	-	*35.7*	*100.0*	2.3	157.8	97	FeO/Cr_2O_3=0.4-1.1	En55, Fs1, Wo44	
A6	*FEI 450*	*1*	*0.2*	*21.1*	*1.0*	*21.6*	*0.2*	*0.5*	-	-	*0.2*	*0.2*	*0.2*	*0.5*	*19.5*	-	-	*34.8*	*100.0*	2.8	6.2	71	Low-Ca Pyroxene	En71, Fs29, Wo0	Enstatite
A7	*FEI 450*	*1*	*0.7*	*17.3*	*1.6*	*24.0*	*0.1*	*0.2*	-	-	*0.2*	*0.1*	*0.7*	*0.3*	*19.3*	-	-	*35.5*	*100.0*	2.6	6.4	67		En67, Fs33, Wo1	
A8	EVO	1	-	16.8	0.7	16.5	0.2	0.4	0.2	-	0.2	-	0.3	-	18.6	-	0.8	37.1	91.8	3.9	7.0	68	Olivine	Fo67, Fa32	Forsterite
A9	*FEI 450*	*1*	-	*29.0*	*0.6*	*19.1*	*0.1*	*0.1*	-	-	*0.1*	-	*1.2*	*0.4*	*8.7*	-	-	*40.7*	*100.0*	3.7	16.4	89		Fo88, Fa11	
A10	EVO	1	-	9.7	2.0	13.4	-	0.2	0.5	-	-	-	0.3	0.2	32.3	-	-	33.2	91.7	4.4	3.6	41		Fo41, Fa59	
A11	*FEI 450*	*1*	*0.3*	*11.1*	*2.5*	*14.6*	-	*0.3*	-	*0.1*	-	*0.3*	*0.1*	*0.2*	*39.6*	-	-	*30.8*	*100.0*	3.7	2.7	39		Fo39, Fa61	Fayalite
A12	*FEI 450*	*1*	*0.2*	*10.4*	*2.8*	*15.1*	-	*0.3*	-	*0.1*	*0.1*	-	*0.5*	*0.4*	*39.7*	-	-	*30.4*	*100.0*	3.5	2.7	38		Fo37, Fa62	
A13	EVO	1	-	6.6	1.7	12.4	-	-	0.1	-	3.1	0.4	-	-	35.4	-	-	31.6	91.3	4.5	3.1	30	Altered CAI	-	Fe-rich phase
A14	*FEI 450*	*1*	*0.2*	*6.9*	*2.7*	*14.5*	-	*0.1*	-	-	*3.8*	*0.4*	*0.2*	*0.3*	*40.4*	-	-	*30.5*	*100.0*	3.7	2.6	28			
A15	*FEI 450*	*1*	*0.0*	*8.6*	*6.2*	*21.8*	-	*0.1*	-	*0.2*	*24.4*	*1.4*	*0.3*	-	*1.5*	-	-	*35.5*	*100.0*	2.9	81.1	93			Ca-rich glass
A16	*FEI 450*	*1*	*0.4*	*11.7*	*2.3*	*26.4*	-	*0.1*	-	-	*17.8*	*0.8*	-	-	*4.4*	-	-	*36.1*	*100.0*	2.4	28.6	86			
A17	EVO	1	-	11.5	1.0	12.5	-	0.8	0.2	-	0.2	-	19.0	7.8	14.5	-	-	39.1	106.5	5.5	9.4	65	Chromite [At% O/Cr = 3.9-6.7]	-	*Overlap with matrix*
A18	FEI 650	-	-	2.7	0.4	4.9	0.1	0.5	-	-	-	-	40.1	6.6	12.3	-	-	47.5	115.0	17.1	13.5	34			
A19	EVO	1	-	7.1	2.0	12.8	-	0.1	-	-	0.7	-	0.3	0.3	39.0	-	-	32.9	95.1	4.5	2.9	29	Fine-grained matrix	-	
A20	EVO	2	-	11.6	1.2	14.3	0.1	0.7	0.3	-	0.2	-	0.6	-	18.9	0.4	0.5	32.1	80.9	3.9	5.9	59			
A21	EVO	2	-	13.7	1.0	12.5	0.3	0.5	0.4	-	0.2	-	0.8	0.1	22.8	0.1	0.8	32.4	85.5	4.6	5.0	58			Dark clast
A22	EVO	8	-	12.5	1.1	13.1	0.2	0.5	0.4	-	0.2	-	0.7	0.1	22.4	0.3	0.6	32.2	84.2	4.3	5.0	56			Average [in spider]
B1	*FEI 450*	*4*	*1.2*	*18.9*	*1.4*	*20.3*	-	*3.2*	-	-	*0.4*	-	*0.3*	-	*20.3*	*0.5*	-	*33.5*	*100.0*	2.89	5.75	68.1	Glass	-	Microchondrule
B2	*FEI 450*	*4*	*0.8*	*10.8*	*1.7*	*12.0*	-	*4.8*	-	-	*1.0*	*0.1*	*0.3*	-	*36.3*	*2.4*	-	*29.9*	*100.0*	4.39	2.86	40.4	Matrix	-	FGR

Fig.1. (A) CP94-050-182, a small (~100µm) Antarctic micrometeorite with a complex formerly hydrated C2 mineralogy. Selected features of interest are shown in B-M and include (B) a microchondrule with a cryptocrystalline texture and thin S-bearing rim, (C) LICE silicates, (D, E, H, I, L and M) relict anhedral silicates with rounded perimeters and mantles of (dehydroxylated) Fe-phyllosilicate, (F) an aqueously altered CAI and (G) a thermally decomposed mass of coarse-grained Fe-phyllosilicate. Also shown are high-magnification regions of the fine-grained matrix, both within the main lithology (J) and the Cr-enriched dark clast (K).

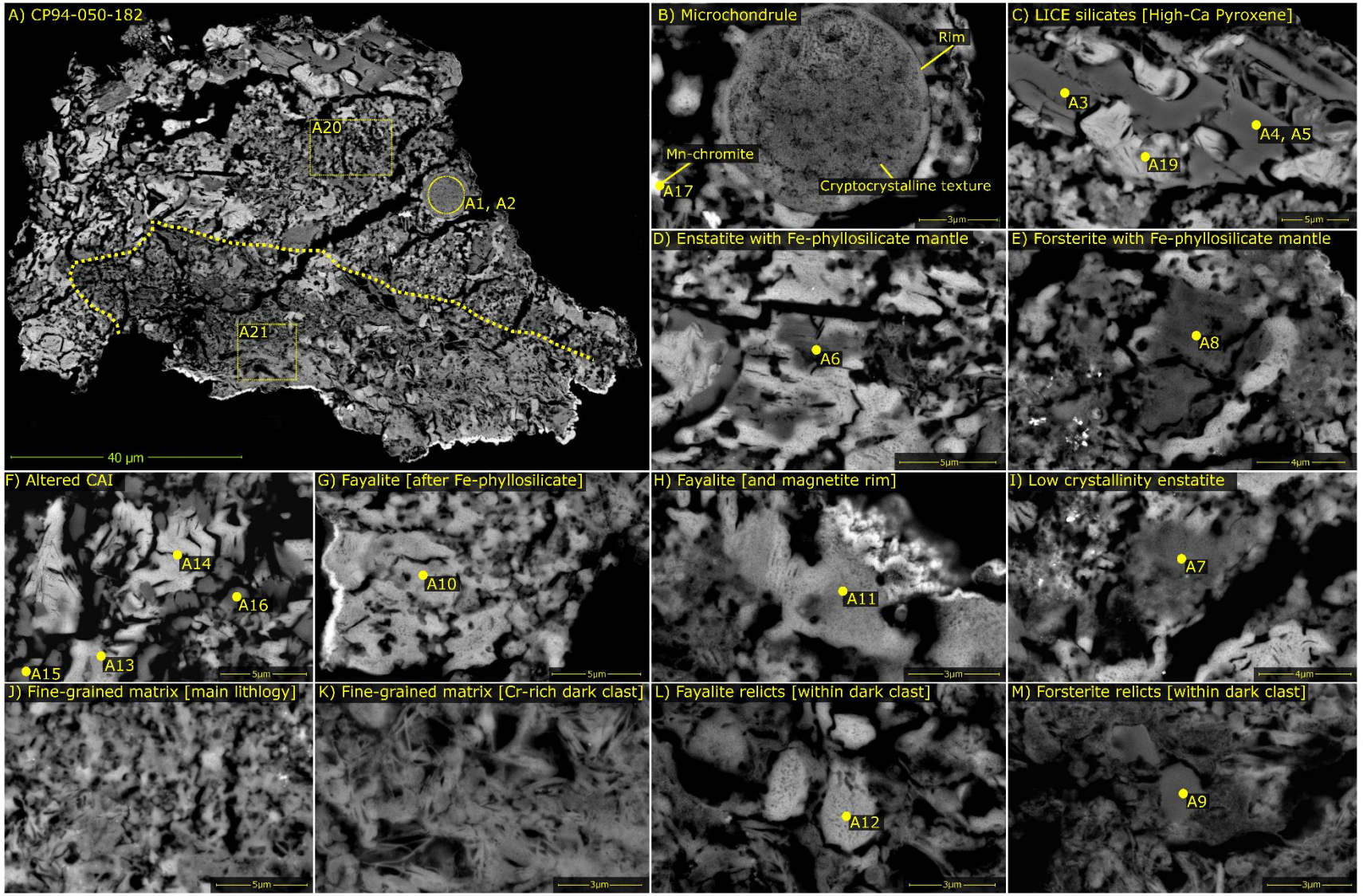

885 **Fig.2**. Whole particle EDS X-ray net intensity maps collected at 12kV. This dataset reveals elemental distribution
886 and partitioning in CP94-050-182. White intensity reflects proportionally higher element concentrations and
887 thereby reveals minerals which are compatible for a given element. A-I show the distributions for Mg, Fe, Si, Al,
888 Ca, K, Cr, Ti and S respectively. The combined high intensity Al, Ca and Ti region (circled in yellow in H) highlights
889 the presence of a refractory inclusions - a CAI that was incompletely replaced by aqueous alteration. Additional
890 features that are visible include: the high-Ca pyroxenes (circled in red in E), the high density of Cr-bearing spinels
891 (circled in blue in G), abundant in the clast, the magnetite rim which lines the particle perimeter and is clearly
892 seen in the Fe map (B) and the striking absence of S (I) from the microchondrule. This hyperspectral dataset was
893 collected at 12kV, with a total analysis time of 60 minutes. Each pixel in this data cube is 0.18µm, the field of
894 view is ~140µm.

895

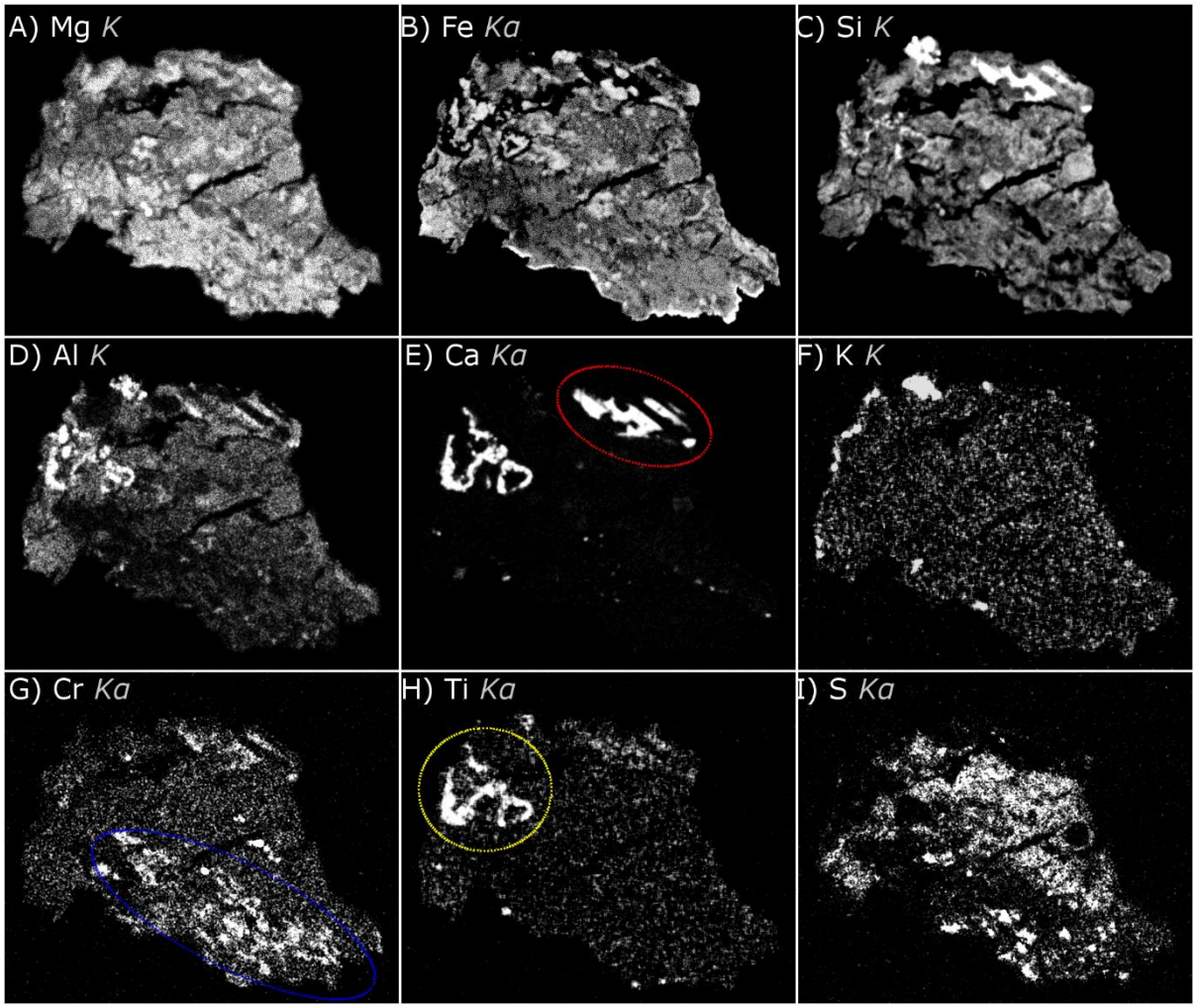

Fig.3. A high spatial resolution (intermediate-voltage [9kV])) elemental net intensity X-ray map. Revealing the distribution and partitioning of elements within the spherical inclusion (microchondrule) and surrounding matrix. Elements A) Mg *Kα*, Fe *L* Ca *Kα*, B) Si *Kα*, S *Kα*, Cr *L* shown, which, with the exception of O and Al, represent the most abundant elements by weight percent within this field of view. This figure highlights geochemical heterogeneities within the chondrule. An irregular-shaped core contains Si and Ca-enrichments, while the chondrule margin is enriched in Fe. A thin sulphur rim mantles the chondrule, this may reflect the leaching of S from the (former) chondrule glass during a later phase of aqueous alteration. B) A *chain* of (Mn and S-bearing) Cr-spinels are seen in the bottom left of the map.

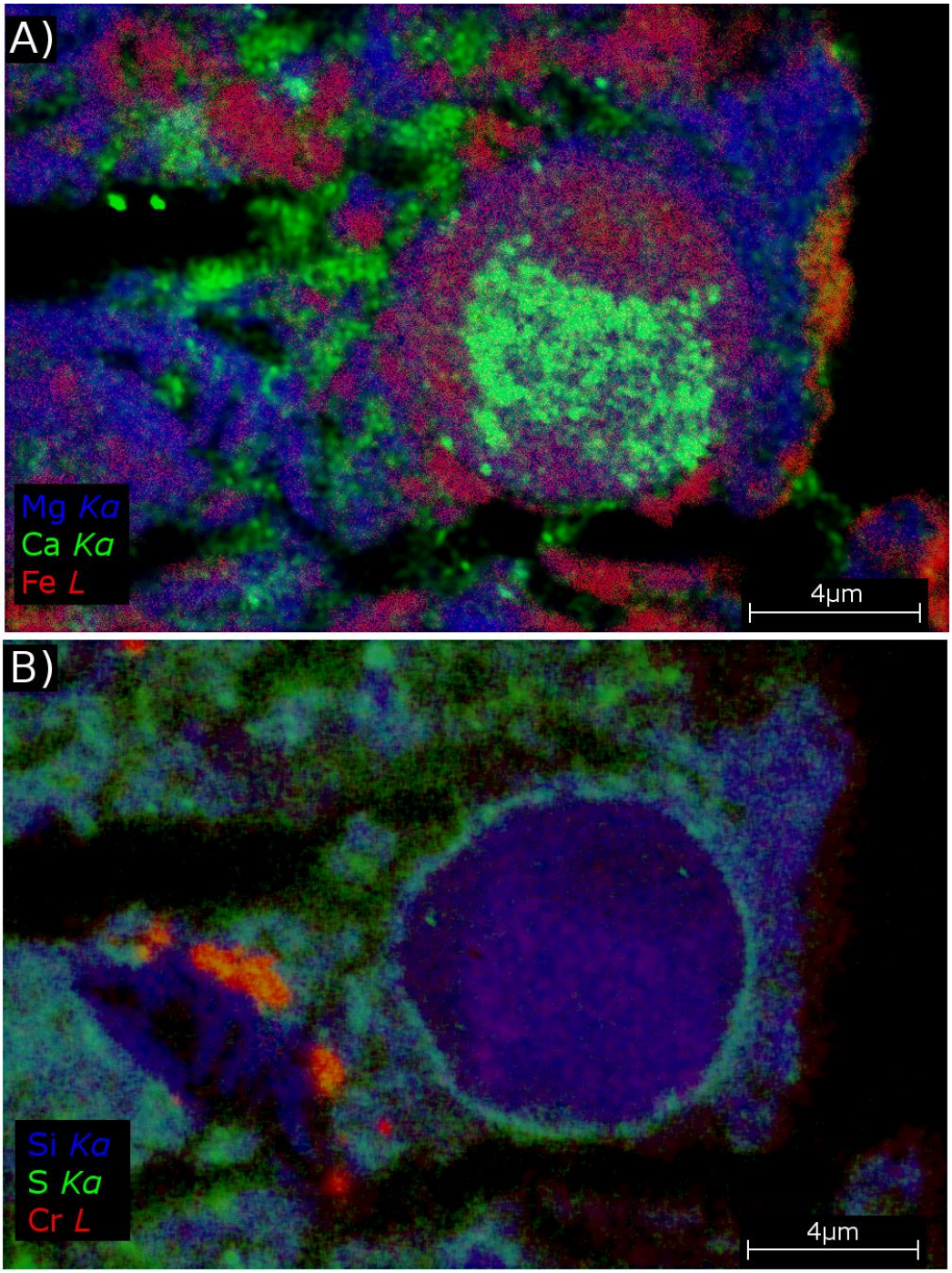

Fig.4. The maximum pixel spectrum – a synthetic energy dispersive spectra – generated from the X-ray element map shown in Fig.3. Constructed by selecting the maximum pixel value within each X-ray energy plane and ignoring the remaining pixels. This spectrum provides a more accurate means of peak identification and is important in identifying trace constituents within an hyperspectral imaging dataset (Bright and Newbury, 2004). Spectrum peaks are labelled with their appropriate elemental signatures. Note, a single peak, located at ~0.3keV and which exceeds 300 counts, is generated by carbon originating from (1) the carbon coat applied to the sample to maintain electrical conductivity, (2) from hydrocarbon contamination arising where the electron beam interacts with trace CO_2 molecules held in the sample chamber and (3) from the excitation of carbon in the epoxy resin medium that holds the micrometeorite. This peak is, therefore, not part of the micrometeorite's mineralogy.

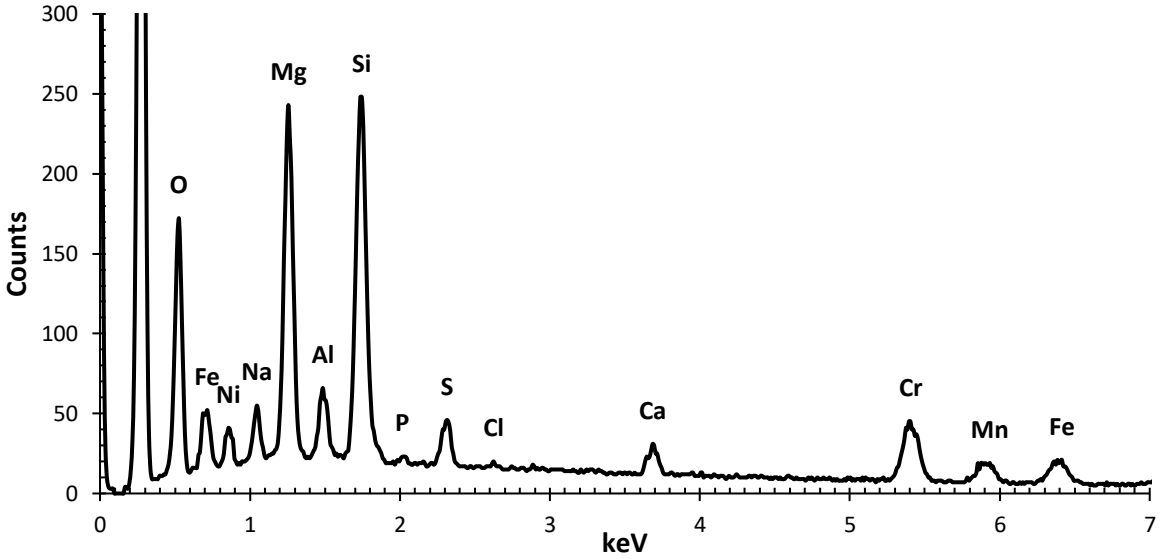

Fig.5. Spider diagrams revealing the particle's (A) bulk composition and (B) the microchondrule composition within CP94-050-182. Bulk compositions for the microchondrule are calculated by standards-based SEM-EDS on the EVO (solid black line) and by standardless EDS after integrating the quantified (intermediate-voltage) X-ray elemental mapping spectra. Elements are ordered by increasing volatility, as defined in Lodders (2003).

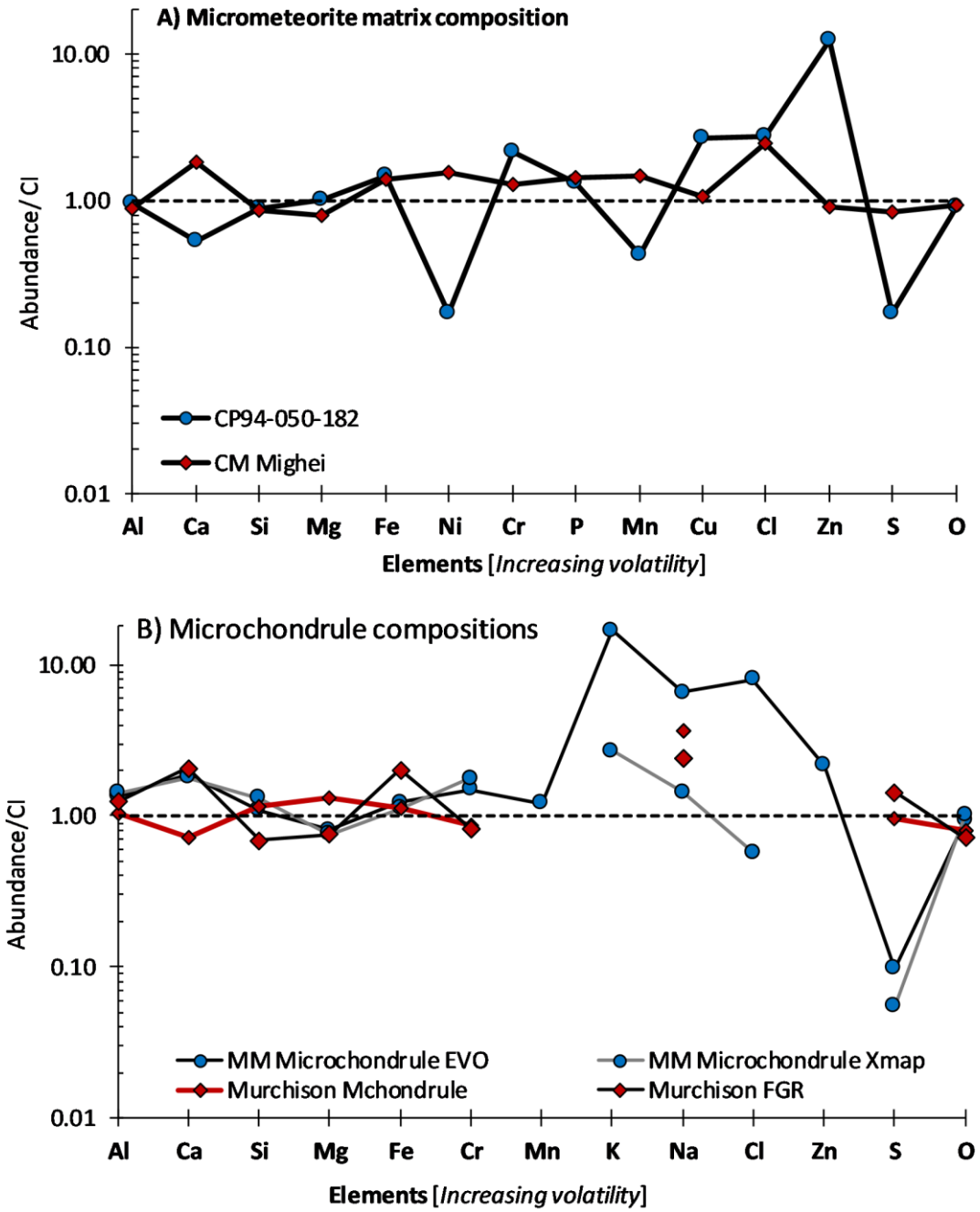

Fig.6. The global mid-IR spectrum (8-13µm) of CP94-050-182, revealing an olivine dominated bulk mineralogy and comparison against olivine mineral standard spectra at the approximate solid solution end members. (Note: Olivine mineral spectra were obtained from the RRUFF database)

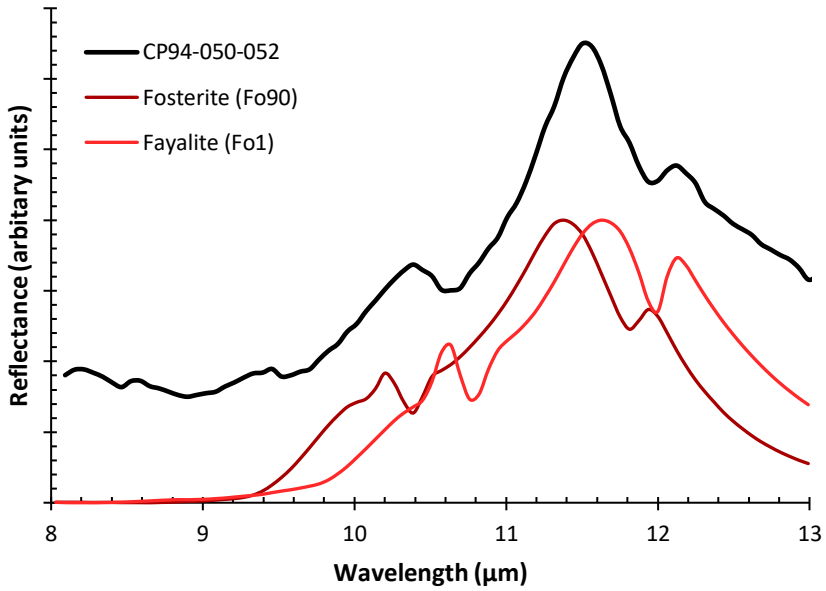

Fig.7. Major-trace element data obtained from high-Ca pyroxene grains found within CP94-050-182. The solid black line, dashed grey line and dotted black line represent the common compositional fields for pyroxene grains found within CM2, CR3 and UOC chondrites, respectively (data taken from Genge, 2008). Both pyroxene grains in CP94-050-182 are distinct from chondritic pyroxenes and instead fall approach the compositions field of low-Fe-Cr-enriched (LICE) and low-Fe-Mn-enriched (LIME) silicates (Klöck et al., 1989; Ebel et al., 2012).

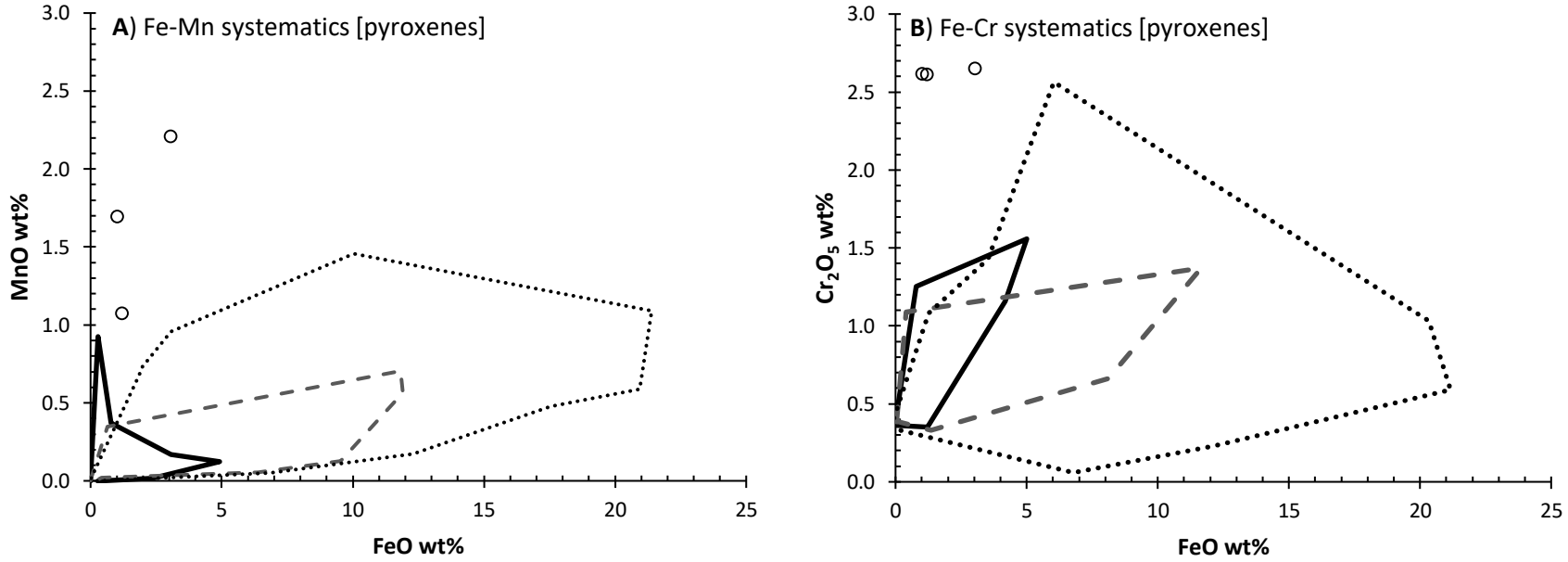

940 **Fig.8.** Fe/(Fe + Mg) versus Cr/(Cr + Al) At% ratios from chromites in ordinary chondrites (grey), CM chondrites
941 (dark blue) and CO chondrites (light blue). Data for CP94-050-182 is shown as EVO data (black cross) and FEI data
942 (black diamond). This figure is adapted after van Ginneken et al., (2012) with data taken from Bunch et al. (1967);
943 Fudali and Noonan (1975); Johnson and Prinz (1991) and Wlotzka (2005).

944

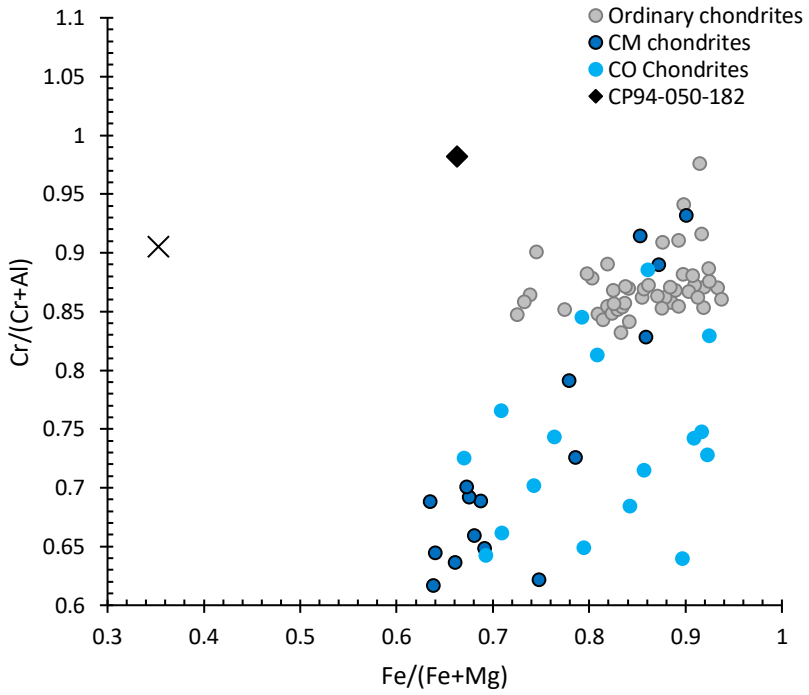

945 **Fig.9.** Geochemical comparison between the micrometeorite-hosted microchondrule analysed in this study
946 (shown as a black cross [EVO data] and a black diamond [FEI QMAP data]) and the bulk compositions of 106
947 glassy (V-type) cosmic spherules (shown in light green) and 76 microchondrules, found within the ordinary
948 chondrites LL3.4 Manych (Dodd, 1978) LL3.0 Semarkona, LL3.15 Bishunpur and the ungrouped 3.05 NWA 5717
949 (Bigolski et al., 2016) [and shown as light grey circles]. The dotted black line delineates the solar ratio as
950 determined by the analysis of CI Ivuna. Elements are ordered by increasing volatility from Al_2O_3 to Na_2O.

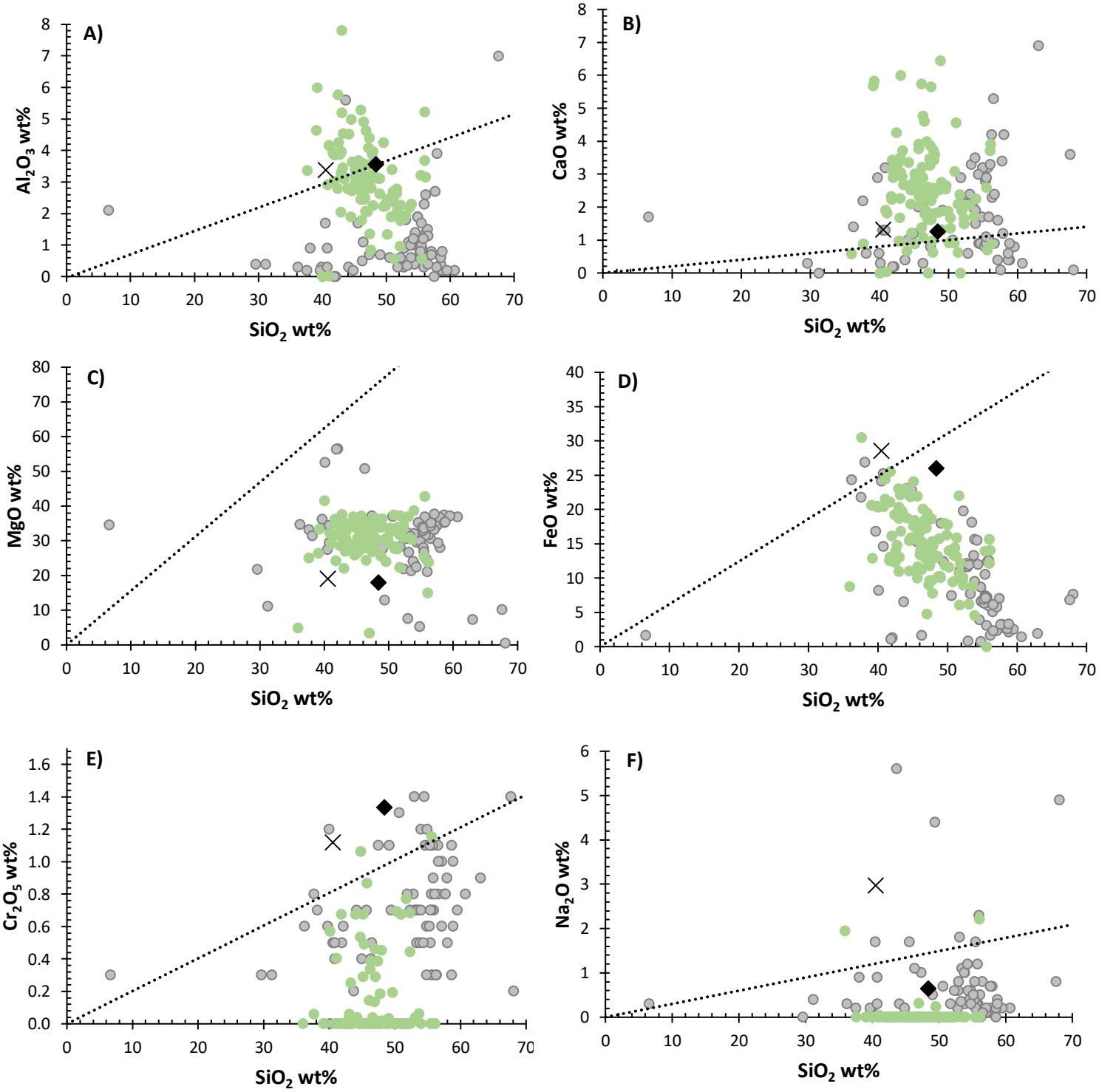

951

952

Fig.10. Microchondrules in CM chondrites, one was found in EET 96029 (A-G) and two were found in Murchison (H-J). All are located within the fine-grained rims of coarse-grained components (either a CAI, chondrule or compound chondrule) and have similar diameters (3-5µm). In EET 96029 the CAI is composed of spinel (dark grey) surrounded by a phyllosilicate rim (white). These microchondrules show weak internal zonation and have glassy textures. TEM data suggest they are composed of poorly crystalline phyllosilicate. Note: panels A, B, H, I and J are SEM-BSE images, panels C, D, E and F are TEM bright-field images, while G is a SAED pattern. Highlighted regions B1 and B2 mark the locations of spot and wide beam EDS analyses (seen in Table.1).

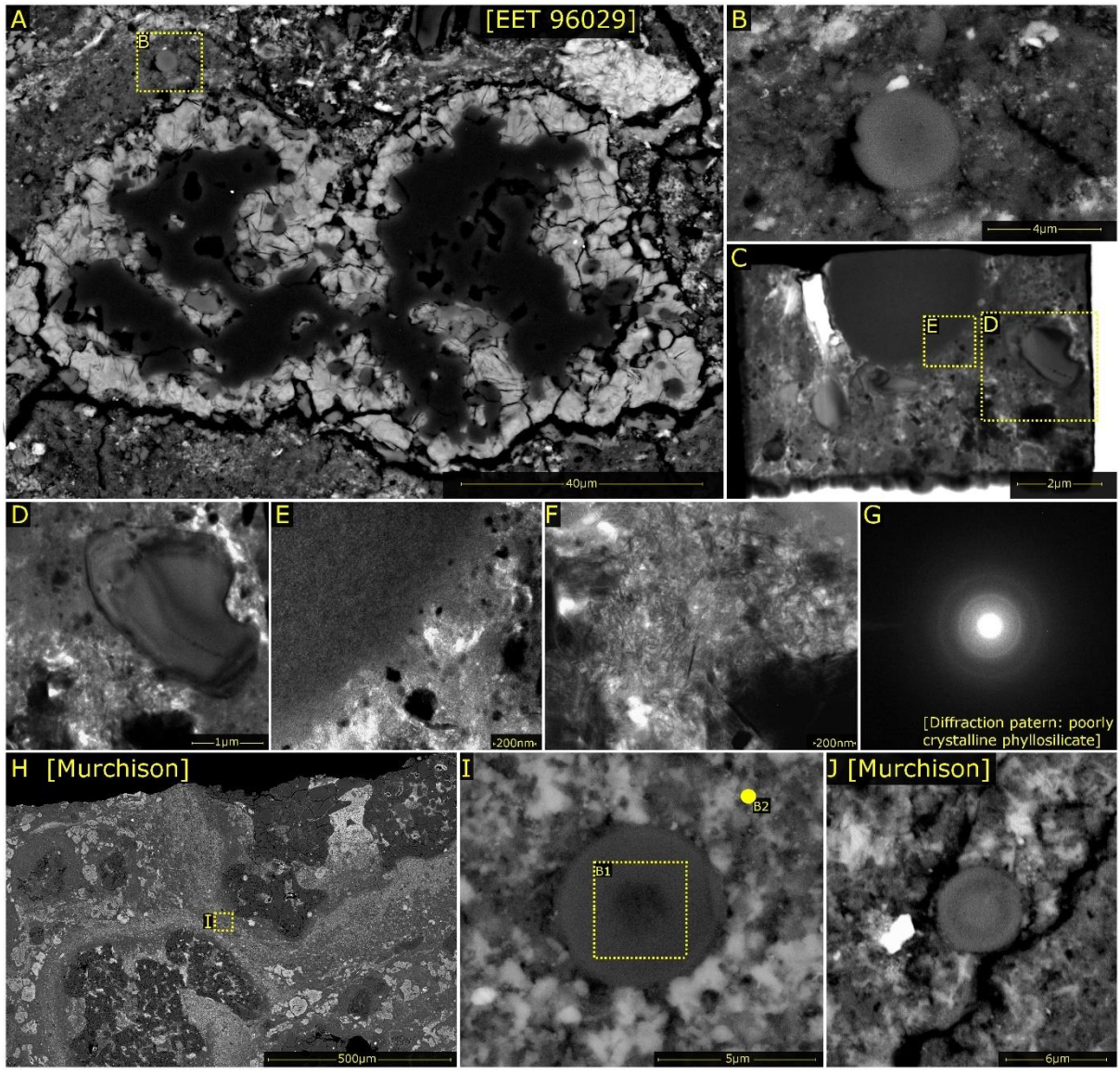

961 **Fig.11**. Large compound chondrules in CM Murchison. In the upper right a compound chondrule containing the
962 studied microchondrule is shown. This object has a complex rim chronology, we have outlined sections of each
963 fine-grained rim to demonstrate successive growth periods. Since some rims are truncated or surround only
964 some of the host chondrules, this requires that rim formation occurred in several distinct stages.

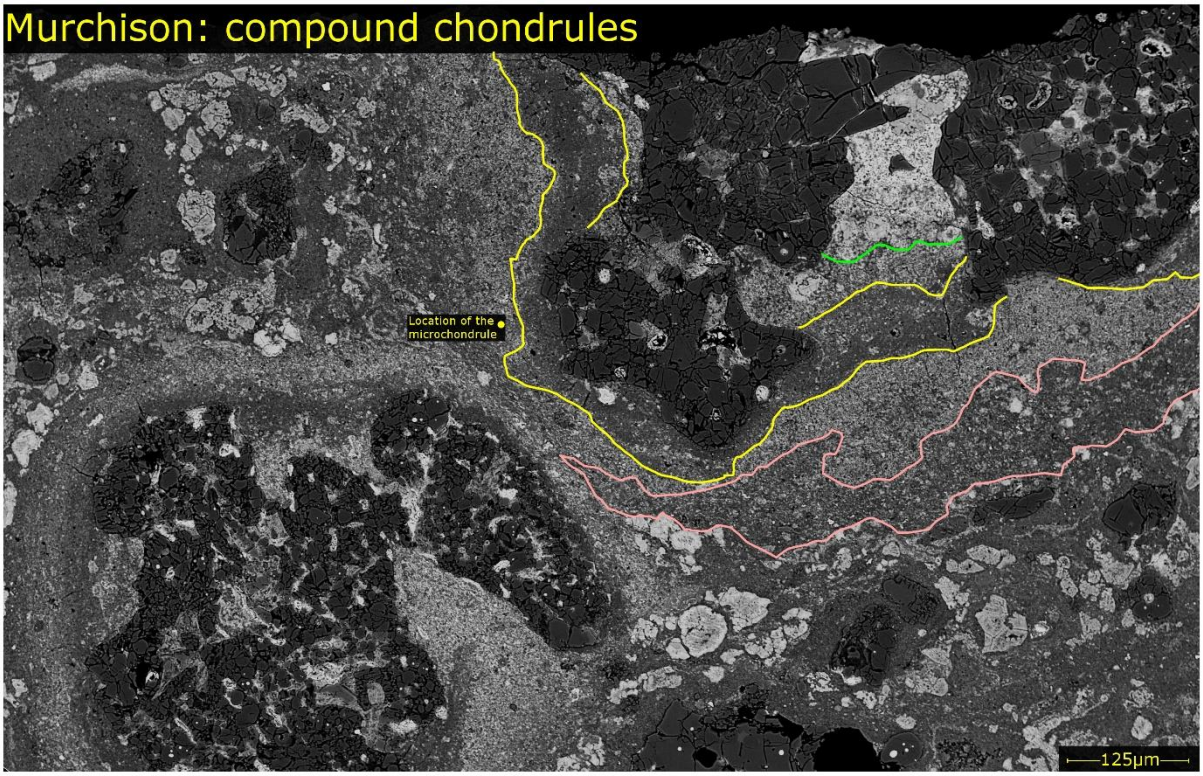

965

966